



# Fe–O–P bond in MIL-88A(Fe)/BOHP heterojunctions as a highway for rapid electron transfer to enhance photo-Fenton abatement of enrofloxacin

Tianyu Wang<sup>a</sup>, Chen Zhao<sup>a,\*</sup>, Linghui Meng<sup>a</sup>, Yujia Li<sup>a</sup>, Dawei Wang<sup>b</sup>, Chong-Chen Wang<sup>a,\*</sup>

<sup>a</sup> Beijing Key Laboratory of Functional Materials for Building Structure and Environment Remediation, Beijing University of Civil Engineering and Architecture, Beijing 100044, China

<sup>b</sup> Key Laboratory of Integrated Regulation and Resource Development on Shallow Lake of Ministry of Education, College of Environment, Hohai University, Nanjing 210098, China

## ARTICLE INFO

### Keywords:

MIL-88A(Fe)  
BOHP  
photo-Fenton  
Charge flow  
Enrofloxacin degradation

## ABSTRACT

MIL-88A(Fe)/BOHP (MxBy) heterojunctions were firstly fabricated via a ball-milling method, which were adopted as catalysts to activate hydrogen peroxide (H<sub>2</sub>O<sub>2</sub>) with the aid of visible light illumination to build a heterogeneous photocatalysis-Fenton-like synergetic system. The catalytic degradation efficiency of enrofloxacin (ENR) (10 mg/L) in the optimal M3B7/Vis/H<sub>2</sub>O<sub>2</sub> system reached nearly 100 % with appreciable mineralization ability. Experimental and theoretical results co-unraveled that the formation of interfacial Fe–O–P chemical bonds between MIL-88A(Fe) and BOHP effectively reduced the charge transfer energy barrier (59.41–26.69 eV) and migration distance (3.104–1.917 Å), allowing the photo-generated carriers to be efficiently separated in space and improving the activation efficiency of H<sub>2</sub>O<sub>2</sub> for producing more active species. Impressively, the constructed M3B7/Vis/H<sub>2</sub>O<sub>2</sub> system was a cost-optimal and green technology for antibiotic wastewater treatment based on Electrical Energy per Order (EE/O) concept, life cycle assessment (LCA) and quantitative structure–activity relationship (QSAR) analysis.

## 1. Introduction

ENR, as a representative fluoroquinolones (FQs) antibiotic, has been extensively employed in treating infections of urinary tract, gastrointestinal system, respiratory tract and dermatosis that caused by Gram-positive and Gram-negative bacteria, due to its stable antibacterial property and broad-spectrum antimicrobial activity [1–3]. Frustratingly, ENR cannot be effectively eliminated through traditional sewage treatments due to its poor biodegradability, which leads to approximately 15–50 % ENR originating from breeding and medical industry ended up in aquatic environments, thereby causing considerable water pollution [4]. More unfortunately, the misuse of ENR will cause the emergence of antibiotic-resistant bacteria (ARB) and antibiotic-resistance genes (ARGs), which can seriously threaten the ecological system and human health [5]. Thus, development of a highly efficient strategy to remove ENR in aquatic environments is urgent.

Traditional Fenton method has been diffusely adopted for homogeneous catalytic degradation of organic contaminants due to its high effectiveness [6]. However, some disadvantages like the need for additional treatments for the dissolved iron ions, an excessive amount of

sludge, and a requirement for acidification (pH = 2–3) might lead to higher costs and potential secondary pollution [7]. Due to its ease of use, mild reaction conditions, and high efficiency, heterogeneous Fenton-like systems over Fe-based catalysts have been used to address the drawbacks of the homogeneous Fenton process [8]. Nevertheless, as for heterogeneous Fe-based catalysts, their catalytic efficiency for decomposition of H<sub>2</sub>O<sub>2</sub> into •OH were directly decided by the amount of exposed active sites and the transformation rate from Fe<sup>3+</sup> to Fe<sup>2+</sup>. As a result, it is important to construct a new Fenton-like reaction system with strong ability to supply electrons. In order to surmount the above-mentioned drawbacks, photocatalysis-Fenton-like synergy system, especially being triggered by visible light irradiation has been attracted considerable attentions [9]. Specifically, the transformation efficiency of Fe<sup>3+</sup> to Fe<sup>2+</sup> can be improved with the assistance of photo-active electrons. In addition, H<sub>2</sub>O<sub>2</sub> as photo-generated electron acceptor can further promote the segregation of electron/hole pairs and induce the production of more reactive oxygen species (ROSs) [10].

Recently, the use of iron-based metal-organic frameworks (Fe-MOFs) for Fenton-like catalysis has received great attention due to the following aspects [11–14]. First of all, the existence of numerous Fe–O

\* Corresponding authors.

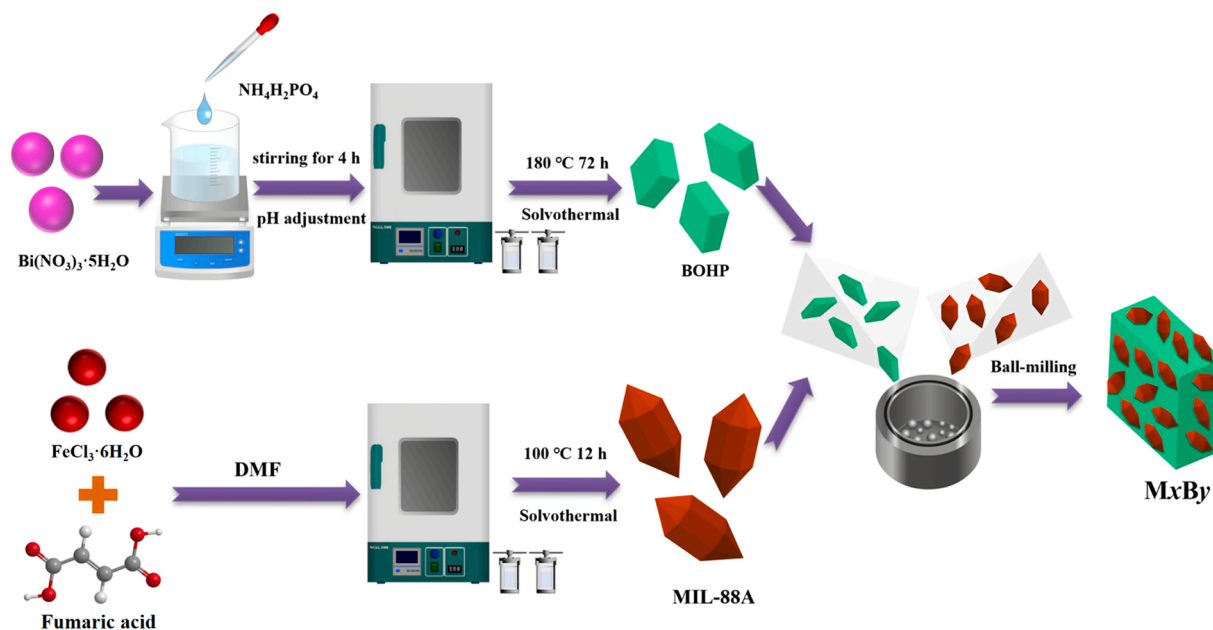
E-mail addresses: [zhaochen1@bucea.edu.cn](mailto:zhaochen1@bucea.edu.cn) (C. Zhao), [wangchongchen@bucea.edu.cn](mailto:wangchongchen@bucea.edu.cn) (C.-C. Wang).

<https://doi.org/10.1016/j.apcatb.2023.122832>

Received 12 January 2023; Received in revised form 13 March 2023; Accepted 30 April 2023

Available online 2 May 2023

0926-3373/© 2023 Elsevier B.V. All rights reserved.



**Scheme 1.** Schematic presentation of the preparation route of MxBy heterojunctions.

clusters display efficient visible light absorption [15]. Secondly, Fe–O clusters are inclined to promote electrons transfer from  $O^{2-}$  to  $Fe^{3+}$ , and then achieve conversion from  $Fe^{3+}$  into  $Fe^{2+}$  in Fe-MOFs. Ultimately, the surface of Fe-MOFs exists abundant coordinatively unsaturated Fe ions, which act as the Lewis acidic sites to adsorb the basic  $H_2O_2$  to generate  $H_2O_2$ -Fe complex and then initiate the production of  $\bullet OH$  [16]. Especially, MIL-88A(Fe) may be classified as an environmentally friendly Fe-MOF constructed from fumaric acid and  $Fe^{3+}$  [17]. With irradiation from visible light, the fumaric acid can contribute electrons to the central Fe ions over the ligand-to-metal charge transfer (LMCT), thus accelerating transformation rate from  $Fe^{3+}$  to  $Fe^{2+}$ . Additionally, MIL-88A(Fe) exhibits comparatively strong reactant transfer ability when compared to the other Fe-MOFs due to the swelling effect of the material, which can cause an increased exposure of active sites and enrich the reaction substrate near the active sites [18]. Nonetheless, the use of pure MIL-88A(Fe) in the photo-assisted Fenton-like process needs to be further refined owing to the simplicity of charge carriers recombination.

Pristine Fe-MOFs incorporated with bismuth-based photocatalysts has been testified to be an effective way for enhancing their corresponding catalytic performances [19,20]. Among them, bismuth oxyhydroxyphosphate ( $Bi_3O(OH)(PO_4)_2$ , BOHP) was firstly reported by Cates's research group [21], possessing practical potential for photocatalytic degradation of perfluoroalkyl substances (PFAS). Its superior UV-light-responsive photocatalytic activity was primarily due to the favorable redox potentials. However, similar with traditional  $TiO_2$  photocatalyst, BOHP can only trigger photocatalytic process under UV light irradiation owing to its large band gap energy ( $\sim 3.90$  eV), resulting in the low utilization of sunlight and limiting its practical application. To best our knowledge, research about expanding the light absorption range of BOHP has not been fully explored. Therefore, based on the inherent merits of MIL-88A(Fe), coupling BOHP with narrow band gap MIL-88A(Fe) to form heterojunction photocatalyst is regarded as a feasible strategy. And it can kill two birds with one stone, first and foremost, the MIL-88A(Fe) spindles could effectively extend the light absorption. In return, BOHP might act as an energy level below the lowest unoccupied molecular orbital (LUMO) of MIL-88A(Fe), leading to more photo-generated electrons to participate the photo-Fenton-like reactions and more ROSs would be produced to attack organic compounds.

In this study, we fabricated MIL-88A/BOHP heterojunctions via ball-milling process, which had been proved as a facile, eco-friendly (minimal solvent or solvent-free), and effective method for preparing heterostructured photocatalysts [22]. The catalytic degradation of ENR was then used to assess the photo-Fenton activities over different MxBy heterojunctions under visible light irradiation. A number of variables, including  $H_2O_2$  concentration, pH, and co-existing substances were extensively investigated. The most important elements responsible for improving the catalytic efficiency were studied via experimental and density functional theory (DFT) calculation results. Additionally, the *EE/O* concept issued by International Union of Pure and Applied Chemistry (IUPAC) was used to calculate the economic viabilities of various catalytic systems. LCA was carried out to evaluate the environmental impacts of different reaction systems. To determine the detoxification ability of developed photo-Fenton-like systems, the degradation pathways and ecotoxicities of ENR degradation products were examined via the LC-MS/MS technique and T.E.S.T. tool.

## 2. Experimental section

### 2.1. Fabrication of MxBy heterojunctions

All chemicals and reagents were utilized without further purification and were listed in Text S1. MIL-88A and BOHP were produced following the previous references with minor modifications (Text S2) [21,23]. The MxBy heterojunctions were fabricated via ball-milling method following the procedure in Scheme 1. Typically, different mass ratios of MIL-88A (Fe) and BOHP (MIL-88A(Fe): BOHP = 1:9, 3:7, 1:1, 7:3, 9:1) were added into a QM-3SP04 ball miller (Nanjing Keyscience Electronic Technology Company). The ball-milling operation was carried out at a rotational rate of 360 rpm for 20 min. The acquired samples with varying mass ratios can be denoted as MxBy. The letters “M” and “B” were abbreviated from MIL-88A(Fe) and BOHP. Meanwhile, the variables “x” and “y” multiplied by 10 were the weight percentages of MIL-88A(Fe) and BOHP accounting for hybrids. Moreover, Electronic Supplementary Information (ESI) Text S3, S4 and S5 showed the details of characterizations, electrochemical measurements and reactive species identification.

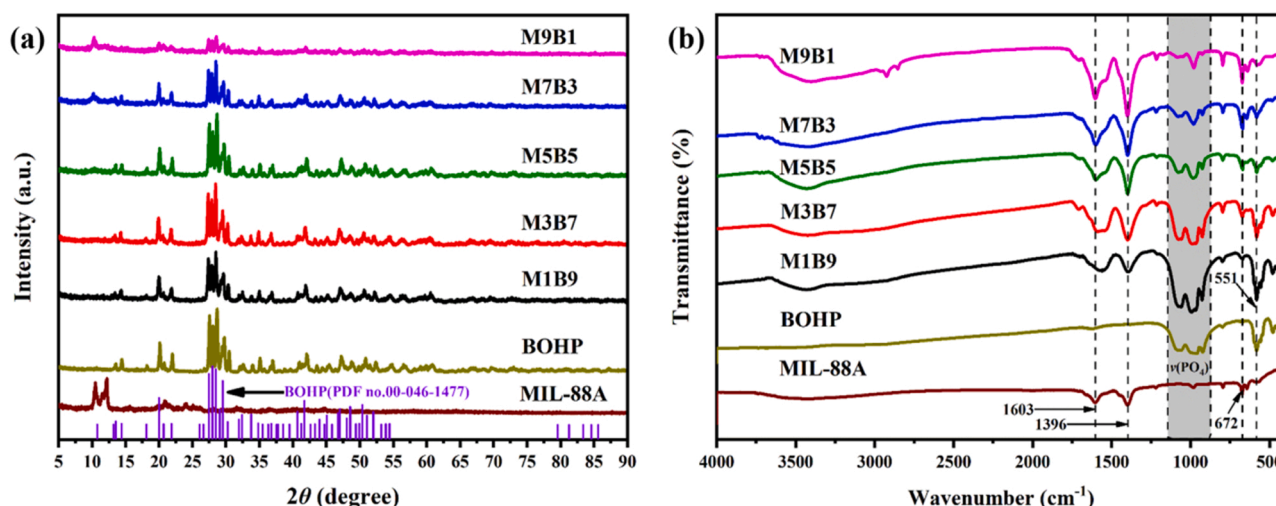


Fig. 1. (a) PXRD patterns and (b) FTIR spectra of the MIL-88A(Fe), BOHP and MxBy samples.

## 2.2. Catalytic degradation of ENR

The degradation of ENR molecules under visible light irradiation was used to evaluate the photo-Fenton-like performances of the MIL-88A(Fe), BOHP, and MxBy samples. Photo-Fenton catalytic tests were performed using a multitube photocatalytic reactor (PCX50C, Beijing Perfectlight Technology Co., Ltd.). The photosource was a  $300 \pm 50$  mW LED lamp. The initial pH of ENR solution was controlled by 2 mol/L of either HCl or NaOH. A specific quantity of catalyst was introduced into 50 mL of ENR aqueous solution with initial concentration of 10 mg/L for each experiment while being magnetically stirred. An adsorption-desorption equilibrium was accomplished in complete darkness prior to the catalytic degradation process. After that, the ENR degradation experiments were started by adding a certain concentration of  $\text{H}_2\text{O}_2$  (1.0, 2.0, 3.0, 5.0 mM) to the reactor so as to search the optimal  $\text{H}_2\text{O}_2$  concentration. 1.5 mL of the mixture was retrieved at pre-determined time and filtered for follow-up analyses using a  $0.22 \mu\text{m}$  Nylon membrane. Subsequently, the optimal concentration of  $\text{H}_2\text{O}_2$  was selected to investigate the effect of initial pH (2.0, 4.0, 6.0, 8.0 and 10.0) on ENR removal. A Vanquish Duo high-performance liquid chromatograph (HPLC, Shimadzu) equipped with a C18 column ( $2.1 \text{ mm} \times 250 \text{ mm}$ ,  $5.0 \mu\text{m}$ ) was employed to monitor the ENR concentrations. The mobile phase was acetonitrile/phosphoric acid with volume fraction of 0.1 % (20/80, v/v) mixture and it flowed at a speed of 0.8 mL/min. The UV detection wavelength and column temperature were set as 280 nm and  $40^\circ\text{C}$ , respectively. An Ultimate 3000 UHPLC-Q-Exactive Orbitrap-MS with a heated electrospray ionization (HESI) source was adopted to record the photodegradation products and the mass spectrum conditions were as follows: ionspray voltage was set as 3.8 kV, capillary temperature was  $300^\circ\text{C}$ , sheath and drying gas flow rates were 40.0 and 10.0 mL/min, respectively. Scan mode was operated as Full MS/dd-MS2. The mass spectra were captured between 50 and 600  $m/z$ . The photo-Fenton-like efficiencies were computed using Eq. 1:

$$\text{Degradation (\%)} = (1 - C_t/C_0) \times 100 \% \quad (1)$$

where the ENR concentrations in the initial and photodegraded specimens at specific withdrawing time were given by  $C_0$  and  $C_t$ , respectively. A TOC tester (Multi N/C 2100 S, Analytik Jena) was applied to monitor the content of total organic carbon (TOC), thereby evaluating the mineralization of ENR.

## 2.3. DFT calculations

All density functional theory (DFT) computations were done using

the Perdew-Burke-Ernzerhof (PBE) formulation under the generalized gradient approximation (GGA). We selected the projected augmented wave (PAW) potentials to describe the ionic cores and took valence electrons into account using a plane wave basis set with a kinetic energy cutoff of 520 eV. Using the Gaussian smearing technique and a width of 0.05 eV, partial occupancies of the Kohn-Sham orbitals were permitted. When the energy shift was less than  $10^{-5}$  eV, the electronic energy was regarded as self-consistent. When the energy variation was less than  $0.05 \text{ eV/\AA}$ , a geometry optimization was deemed to have reached convergence. In our structure, the U correction was used for Fe atoms. The Brillouin zone integration was performed using  $2 \times 2 \times 1$  Monkhorst-Pack  $k$ -point sampling for a structure.

## 3. Results and discussion

### 3.1. Characterization

#### 3.1.1. Powder X-ray diffraction (PXRD) and fourier transform infrared (FTIR) analysis

Fig. 1 showed the PXRD patterns of the MIL-88A(Fe), BOHP, and MxBy samples. MIL-88A(Fe) was successfully obtained in this investigation, as evidenced by the primary diffraction peaks of its virgin form, which were in agreement with the findings in our previous publication [23]. In terms of BOHP, its conspicuous diffraction peaks can be observed at  $14.4^\circ$ ,  $20.0^\circ$ ,  $27.4^\circ$ ,  $34.8^\circ$  and  $41.7^\circ$ , which respectively correspond to (0 0 1), ( $-2$  0 1), ( $-2$  0 2), (1  $-1$  2) and (3 0 1) planes of the triclinic crystal system of BOHP (PDF No.00-046-1477) [21]. By contrast, the diffraction peaks of BOHP in MxBy samples could be clearly observed, indicating that the crystal texture of BOHP was not damaged after being incorporated with MIL-88A(Fe) via ball-milling process. Additionally, the characteristic peaks of MIL-88A(Fe) became more distinct by raising the content of MIL-88A(Fe) in the MxBy heterojunctions.

In this investigation, FTIR spectra of the fabricated catalysts were also analyzed to further affirm the successful preparation of the heterojunction between MIL-88A(Fe) and BOHP. Fig. 1b demonstrated that the usual peaks at  $1603 \text{ cm}^{-1}$  and  $1396 \text{ cm}^{-1}$  in MIL-88A(Fe) were related to the stretching vibrations of C=C or C=O in carboxyl moiety [24]. The stretching vibration at  $672 \text{ cm}^{-1}$  may be ascribed to the vibration mode of Fe-O [25]. The peak at  $551 \text{ cm}^{-1}$  was presumably arising from BOHP and should be indexed to the stretching vibration of the Bi-O bond [26]. The characteristic bands around  $1000 \text{ cm}^{-1}$  could be assigned to phosphate [27]. In addition, all the characteristic absorption bands assigned to MIL-88A and BOHP appeared in the spectra of the MxBy samples, demonstrating the successful combination of two

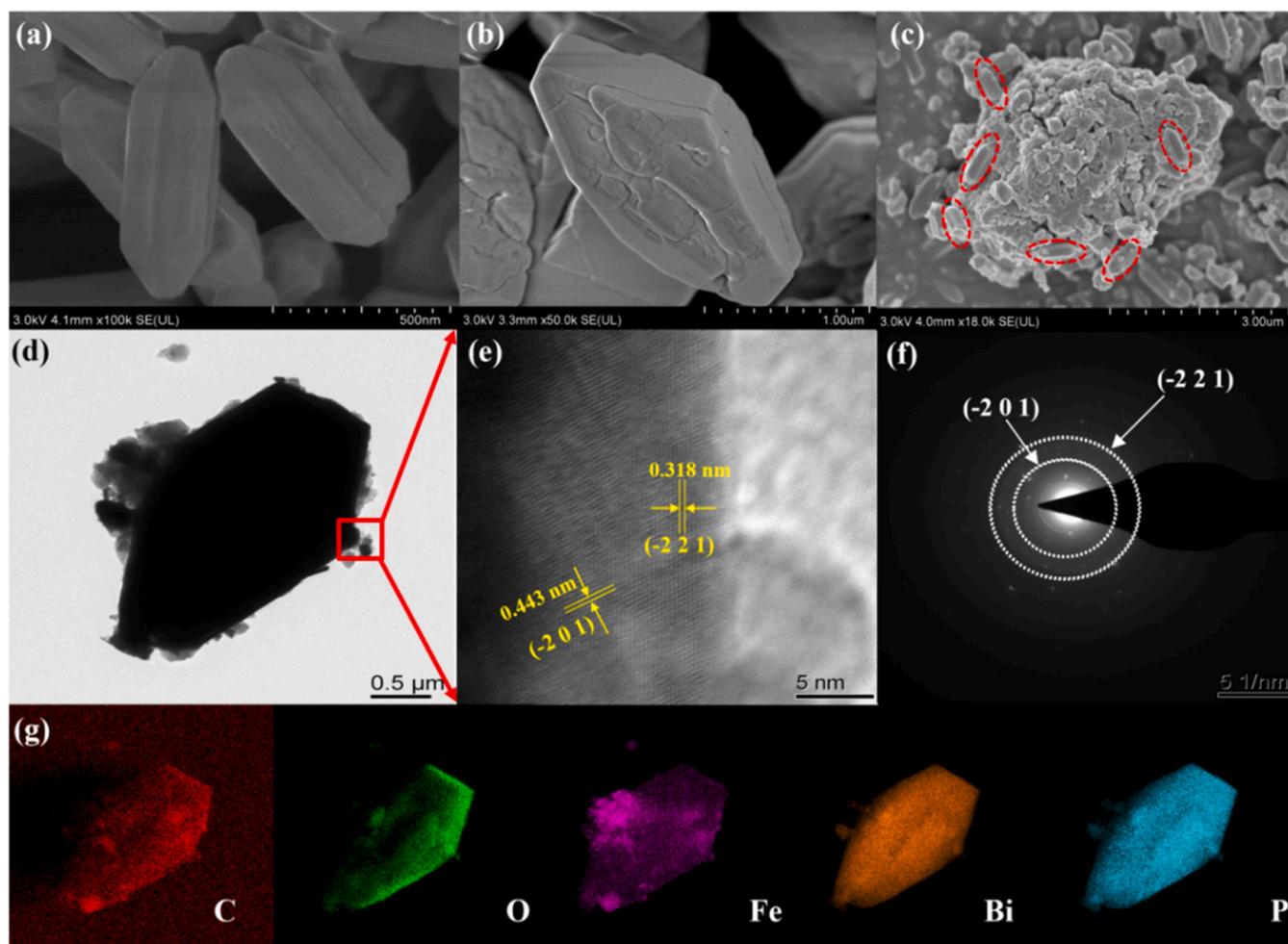


Fig. 2. SEM micrographs of (a) MIL-88A(Fe), (b) BOHP, (c) M3B7, (d)-(e) HRTEM micrographs, (f) SAED pattern and (g) EDS mapping images of the as-prepared M3B7 sample.

components.

### 3.1.2. Morphology observation

The microstructures of the MIL-88A(Fe), BOHP and M3B7 (representative sample of the  $M_xB_y$  heterojunctions) were probed via scanning

electron microscope (SEM), high-resolution transmission electron microscope (HRTEM) as shown in Fig. 2. The MIL-88A(Fe) possessed smooth spindle-shaped morphology with diameters of 500–1000 nm, which was in keeping with our published data [23]. The pristine BOHP structure had a regular rhombohedral morphology with crystallite size

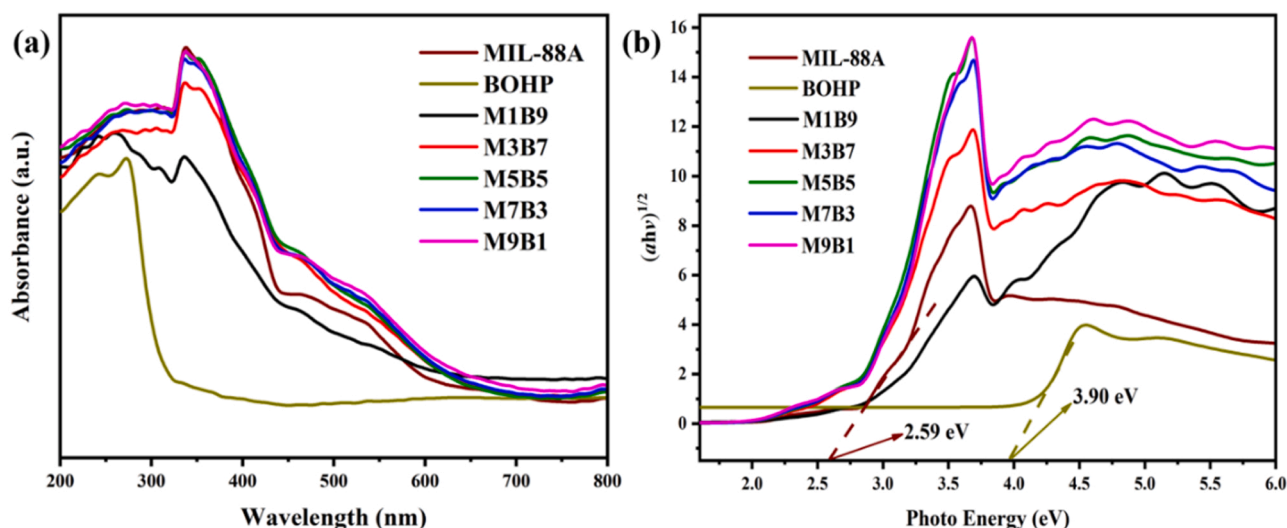


Fig. 3. (a) Diffuse reflectance UV-vis DRS spectra and (b) band gap determination plots of BOHP, MIL-88A(Fe) and  $M_xB_y$  heterojunctions.



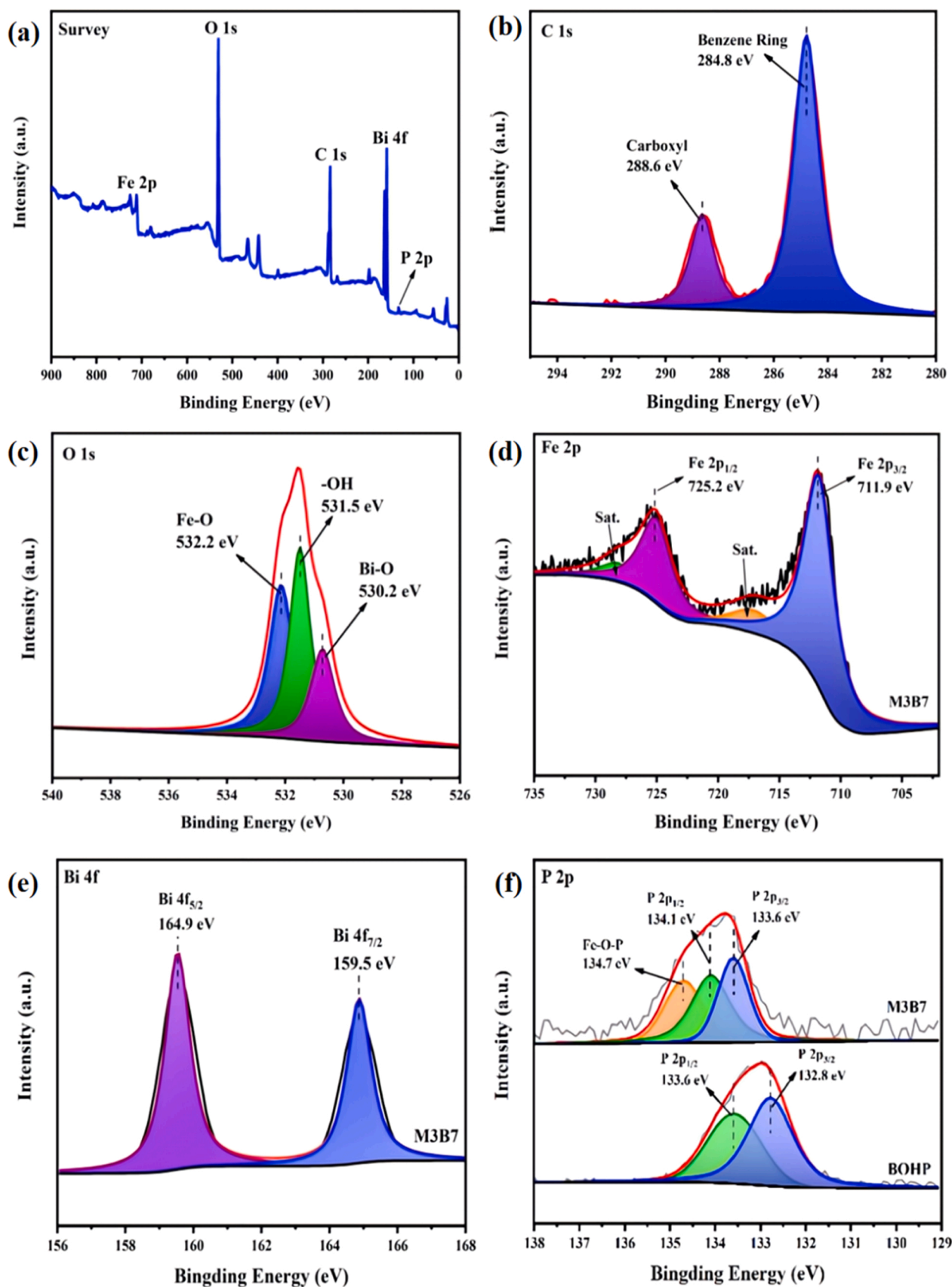
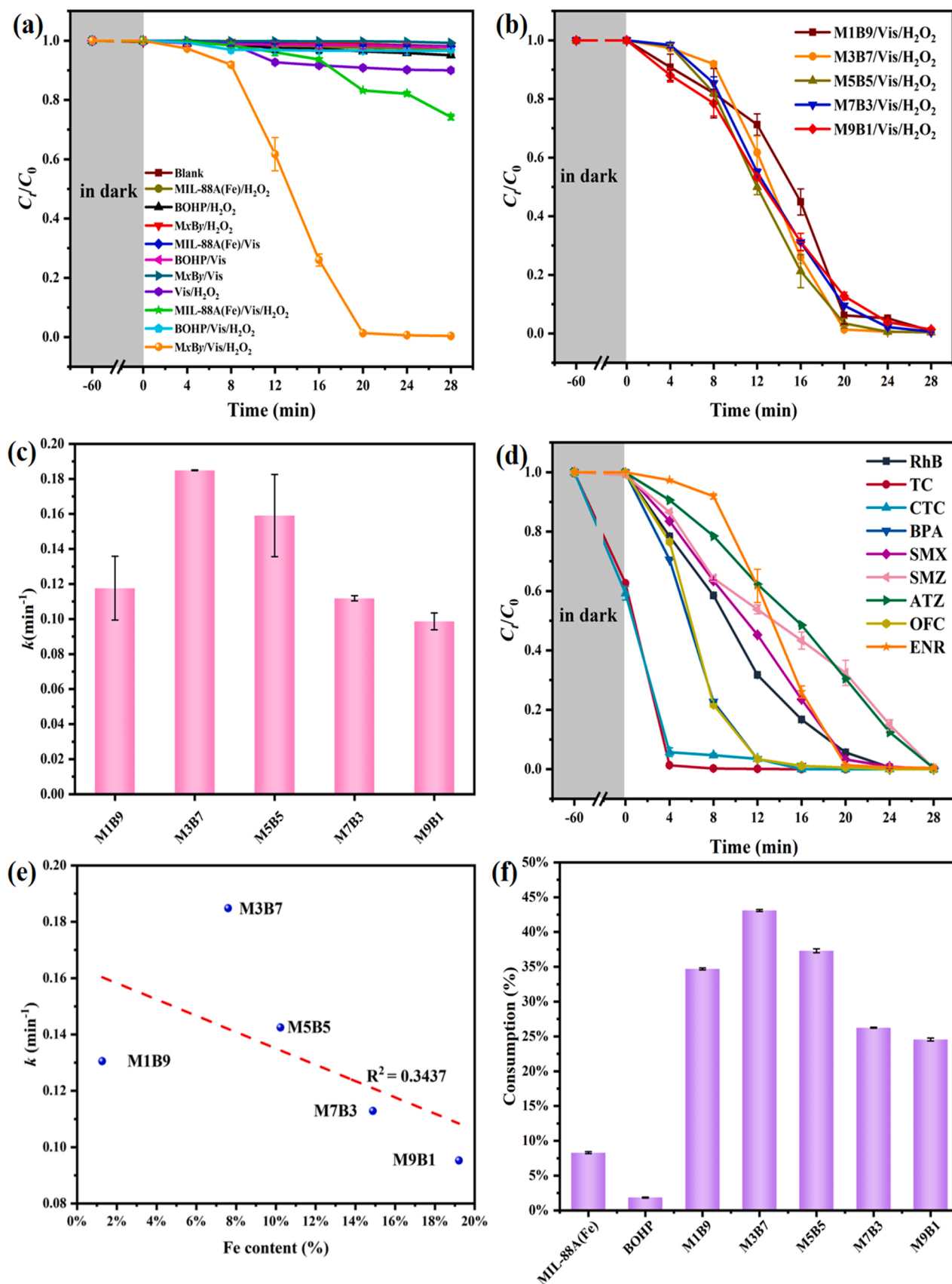


Fig. 4. XPS spectra of the as-prepared M3B7 sample. (a) survey scan, (b) C 1s, (c) O 1s, (d) Fe 2p, (e) Bi 4f and (f) the comparison of P 2p spectra between BOHP and M3B7.



**Fig. 5.** (a) Time-dependent photo-Fenton degradation of ENR over different reaction systems, (b)-(c) the ENR degradation performances and pseudo-first-order kinetic rates in different MxBy/Vis/H<sub>2</sub>O<sub>2</sub> systems, (d) catalytic degradation of different types of organic pollutants in the M3B7/Vis/H<sub>2</sub>O<sub>2</sub> system. Condition: catalyst = 0.4 g/L, pH = 6.0, H<sub>2</sub>O<sub>2</sub> = 3.0 mM, the concentrations of all organic pollutants were 10 mg/L, (e) the correlation between pseudo first-order kinetic constants and Fe contents in different catalysts, and (f) H<sub>2</sub>O<sub>2</sub> consumption in different catalytic systems.

of 1.5–3  $\mu\text{m}$  in length (Fig. 2b). Following the combination, it was clearly evident that the MIL-88A(Fe) spindles were randomly stacked on the surfaces of BOHP (Fig. 2c). In addition, the HRTEM micrograph (Fig. 2d) displayed the tightly interfacial contact between BOHP and MIL-88A(Fe), demonstrating that the heterostructure had been successfully fabricated. According to Fig. 2e, the lattice fringes of the M3B7 sample had high BOHP crystallinity, measuring 0.318 nm and 0.443 nm, and respectively related to the  $(-2\ 2\ 1)$  and  $(-2\ 0\ 1)$  planes of BOHP (PDF no.00-046-1477). Meanwhile, the  $(-2\ 0\ 1)$  and  $(-2\ 2\ 1)$  planes of BOHP should be credited for creating the polycrystalline diffraction rings in the SAED (Fig. 2f). In addition, EDS-mapping images were performed to reveal elemental distribution of the M3B7, it was not hard to find that the Bi, O and P elements were all identified and manifested a homogeneous distribution in the M3B7 sample, while Fe and C were primarily gathered in the MIL-88A(Fe) component, revealing that MIL-88A(Fe) spindles were loaded on the BOHP after the ball-milling process. The above results indicated that the microstructure of close contact was generated between MIL-88A(Fe) and BOHP in M3B7 sample, which was expected to facilitate the transportation of photo-generated charge carriers and eventually to boost the catalytic performance.

### 3.1.3. Ultraviolet-visible diffuse reflectance (UV-vis DRS) analysis

Optical analysis was used to explore the light absorption characteristics of the as-prepared materials. As illustrated in Fig. 3a, the maximum absorption wavelength of pristine BOHP was approximately 285 nm and demonstrated that BOHP could only exhibit a response to UV light. By contrast, MIL-88A(Fe) exhibited an obvious enhancement of visible light absorption at 200–600 nm, which should be attributed the LMCT process of  $\text{O}^{\text{II}} \rightarrow \text{Fe}^{\text{III}}$  and the presence of  $\text{Fe}_3\text{O}$  clusters in Fe-based MOF [28]. Notably, the visible light absorption intensities were improved after incorporation to MIL-88A(Fe) in the MxBy heterojunctions, indicating that the binary structure in the MxBy samples might produce photo-generated charge carriers under visible light illumination and was beneficial to enhancement of their catalytic activities. Moreover, the band gaps ( $E_g$ ) of the catalysts were calculated by Kubelka-Munk function as expressed in Eq. 2 [29]:

$$\alpha h\nu = A(h\nu - E_g)^{n/2} \quad (2)$$

where  $a$ ,  $\nu$ ,  $h$ , and  $A$  respectively referred to the absorption coefficient, frequency of light, Planck's constant, and a constant. The  $n$  values were decided by their transition properties ( $n = 4$  or  $1$  stand for indirect transition or direct transition). Therefore, the  $E_g$  values of M1B9, M3B7, M5B5, M7B3, and M9B1 were determined as 2.78, 2.7, 2.67, 2.65 and 2.63 eV, respectively (Fig. 3b). Although the  $E_g$  values of the MxBy samples were larger than the pristine MIL-88A(Fe) (2.59 eV), they were still much less than the BOHP (3.90 eV), which could enhance their responsiveness for visible light source.

### 3.1.4. X-ray photoelectron spectra (XPS) analysis

XPS spectra were utilized to further detect the chemical valance states of M3B7 sample. The whole XPS survey spectrum of M3B7, as shown in Fig. 4a, revealed the existence of C, O, Fe, Bi and P elements, which correlated well with the EDS mapping analysis. Fig. 4b-f displayed high-resolution C 1s, O 1s, Fe 2p, Bi 4f, and P 2p spectra in the M3B7. Two unique peaks in the C 1s spectra were visible at 288.6 and 284.8 eV, which were ascribed to the  $\text{O}-\text{C}=\text{O}$  and  $\text{C}-\text{C}$  bonds formed by fumaric acid in MIL-88A(Fe), respectively [30,31]. Three peaks at 532.2, 531.5, and 530.2 eV obtained from the deconvolution of the O 1s spectra of the M3B7 in Fig. 4c might be attributable to  $\text{Fe}-\text{O}$ ,  $-\text{OH}$ , and  $\text{Bi}-\text{O}$  bonds, respectively. [32–34]. The high-resolution Fe 2p spectrum for the M3B7 in Fig. 4d could be fitted into two peaks located at 711.9 and 725.2 eV, which can be respectively indexed to Fe  $2p_{3/2}$  and Fe  $2p_{1/2}$  [35]. In addition, the two distinct peaks at 717.7 eV and 728.6 eV were commonly related to the satellite peak of Fe  $2p_{3/2}$  and Fe  $2p_{1/2}$ . In a

word, the four peaks demonstrated the existence of  $\text{Fe}^{3+}$  ions. Additionally, Fig. 4e displayed two characteristic peaks in the Bi 4f high-resolution spectra at 164.9 eV and 159.5 eV, which were ascribed to Bi  $4f_{5/2}$  and Bi  $4f_{7/2}$ , demonstrating the presence of  $\text{Bi}^{3+}$  in the BOHP component [36]. Meanwhile, the P 2p spectrum of pristine BOHP (Fig. 4f) showed a pair of distinctive peaks at 132.8 eV and 133.6 eV, corresponding respectively to P  $2p_{3/2}$  and P  $2p_{1/2}$  [37]. By comparison, it could be seen that the spectrum of P 2p presented distinctly shift to the higher energy region after compounding with MIL-88A(Fe), suggesting that the existence of interfacial interaction between BOHP and MIL-88A(Fe). Furthermore, a novel characteristic peak at 134.7 eV in M3B7 could also be observed, which was presumably ascribed to the generation of  $\text{Fe}-\text{O}-\text{P}$  bond [38]. Previous studies suggested that constructing atomic-level charge-transfer channels at heterojunction interface could tremendously facilitate vectorial migration of photo-generated charge at the formed interface and decrease the transmission distance as well as energy barrier of electron transfer, thereby drastically elevating catalytic performance [39,40].

### 3.2. Evaluation of catalytic performance

The photo-Fenton-like performances of the as-prepared catalysts were firstly estimated by ENR removal under visible light illumination. First of all, as illustrated in Fig. 5a, it was apparently that the self-degradation of ENR upon visible light illumination was negligible. Moreover, the extremely low removal efficiency of ENR with the assistance of visible light and  $\text{H}_2\text{O}_2$  could be related to the small quantities of ROSs like  $\bullet\text{OH}$  radicals were produced during direct photolysis of  $\text{H}_2\text{O}_2$ . Under visible light irradiation, only 3.6 % of ENR molecules were degraded by M3B7/Vis systems, indicating that the sole photocatalytic reaction system did not achieve satisfactory ENR removal efficiency. Meanwhile, the constructed heterogeneous Fenton reaction systems were also not competent for the catalytic degradation of ENR, only 4.1 %, 1.3 % and 4.2 % of ENR molecules were decomposed through MIL-88A(Fe)/ $\text{H}_2\text{O}_2$ , BOHP/ $\text{H}_2\text{O}_2$  and M3B7/ $\text{H}_2\text{O}_2$  systems, respectively. However, compared with the photocatalysis and heterogeneous Fenton reactions, the catalytic performances had a significantly improvement in photo-Fenton-like synergetic systems. Specifically, being compared to the MIL-88A(Fe)/Vis/ $\text{H}_2\text{O}_2$  (24.8 %) and BOHP/Vis/ $\text{H}_2\text{O}_2$  (3.5 %) systems, the M3B7/Vis/ $\text{H}_2\text{O}_2$  reaction system showed the highest ENR removal efficiency (99.9 %) after 28 min of catalytic process. This experimental phenomenon indicated that luminous energy can substantially facilitate the Fenton-like reaction between M3B7 and  $\text{H}_2\text{O}_2$ . More importantly, about 40 % of TOC removal was attained in 120 min in the M3B7/Vis/ $\text{H}_2\text{O}_2$  system (as depicted in Fig. S1), revealing that the MxBy heterojunctions were high-efficiency Fenton-like catalyst.

To further evaluate the superiority of MxBy as photo-Fenton catalysts, a number of photo-Fenton-like experiments were carried out utilizing various catalysts for the purpose of comparison. As illustrated in Fig. 5b, greater than 99 % of ENR could be decomposed by different MxBy/Vis/ $\text{H}_2\text{O}_2$  systems within 28 min of irradiation time. Meanwhile, the enhanced photo-Fenton-like catalytic mechanism was studied by kinetic analysis, and the reaction rate constants ( $k$ ) were acquired by pseudo-first-order kinetic equation ( $\ln(C/C_0) = -kt$ ) [41]. As illustrated in Fig. 5c, the  $k$  values corresponding to M3B7/Vis/ $\text{H}_2\text{O}_2$  system was  $0.185 \pm 0.00001\text{ min}^{-1}$ , which was 23.125 and 102.778 times higher than those of MIL-88A(Fe)/Vis/ $\text{H}_2\text{O}_2$  ( $0.008 \pm 0.00004\text{ min}^{-1}$ ) and BOHP/Vis/ $\text{H}_2\text{O}_2$  systems ( $0.0018 \pm 0.00001\text{ min}^{-1}$ ), respectively. With regard to MxBy/Vis/ $\text{H}_2\text{O}_2$  systems, their dynamic constants were arranged in the following order: M9B1 ( $0.099 \pm 0.00482\text{ min}^{-1}$ ) < M7B3 ( $0.112 \pm 0.00147\text{ min}^{-1}$ ) < M1B9 ( $0.118 \pm 0.01824\text{ min}^{-1}$ ) < M5B5 ( $0.159 \pm 0.02348\text{ min}^{-1}$ ) < M3B7 ( $0.185 \pm 0.00019\text{ min}^{-1}$ ). The above results suggested that optimum mass ratio of MIL-88A(Fe) in MxBy heterojunctions was 30 %, much more MIL-88A(Fe) components might result in reducing the active sites and inhibiting photo-generated electron-hole transfer between the formed interfaces [42]. Furthermore,

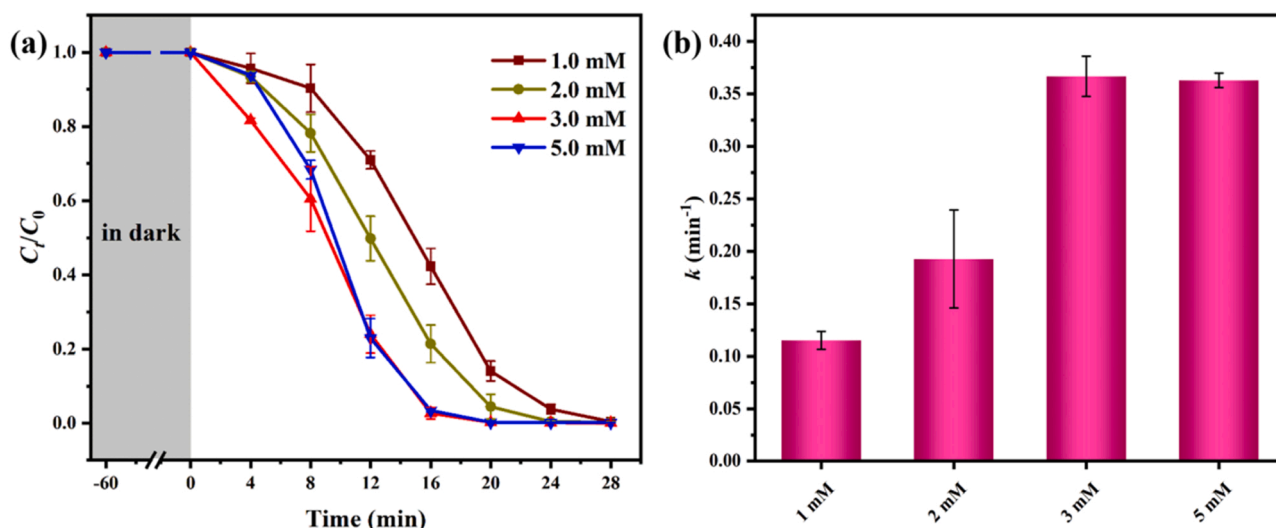


Fig. 6. (a) Impact of  $H_2O_2$  concentration on the ENR removal, (b) the corresponding  $k$  values. Condition: ENR = 10 mg/L, M3B7 = 0.4 g/L, pH = 6.0.

rhodamine B (RhB), tetracycline (TC), chlortetracycline (CTC), bisphenol A (BPA), sulfamethazine (SMZ), sulfamethoxazole (SMX), ofloxacin (OFC) and atrazine (ATZ) were also selected as the contaminant models in water environments to investigate the catalytic degradation performances of M3B7/Vis/ $H_2O_2$  reaction system. It was observed in Fig. 5d that all the organic pollutants can be effectively removed within 28 min over the constructed M3B7/Vis/ $H_2O_2$  reaction system, indicating that it possessed broad application prospects.

It had been reported that the amount of Fe species could significantly influence the efficiency of heterogeneous Fenton-like reaction [43]. To evaluate effect of Fe species in MxBy heterojunctions on ENR degradation process, ferric content within the catalyst was estimated by the Inductively Coupled Plasma (ICP) technique. The outcome implied that ferric content within M1B9, M3B7, M5B5, M7B3 and M9B1 were 1.27, 7.60, 10.23, 14.88, and 19.21 wt %, respectively. Obviously, ferric content in the catalyst was found to be negatively correlated with the degradation rate ( $R^2 = 0.3437$ ) through data fitting (Fig. 5e), indicating that photocatalysis mediated generation of photo-generated electrons and holes played dominant roles in ENR removal, rather than heterogeneous Fenton reaction driven by active Fe species on the surfaces of

MxBy heterojunctions. Moreover, the utilization efficiency of  $H_2O_2$  was ascertained by DMP (2,9-dimethyl-1,10-phenanthroline) method [44]. The details of the method were described in ESI Text S6. As shown in Fig. 5f, the  $H_2O_2$  consumption efficiency over the M3B7/Vis/ $H_2O_2$  system was highest (42.88 %), which should be attributed to more photo-generated electrons were produced in the M3B7 heterojunction under visible light irradiation. Afterwards, the accumulated electrons might react with  $H_2O_2$  to form more reactive ROSs, thereby enhancing the photo-Fenton catalytic activity.

### 3.2.1. Effect of $H_2O_2$ concentration

Because of its direct relation to the quantity of reactive radicals, the concentration of  $H_2O_2$  introduced into the aqueous solution is a significant factor in the photo-Fenton-like process [45]. In the second place, adding  $H_2O_2$  as an electron acceptor is conducive to accelerate electron-hole separation to enhance the catalytic efficiency [46]. This study looked into the impact of  $H_2O_2$  concentrations ranging from 1.0 to 5.0 mM on the catalytic oxidation of ENR. As depicted in Fig. 6a, the ENR removal efficiency increased when the  $H_2O_2$  concentration was increased from 1.0 to 3.0 mM. The corresponding  $k$  values went up from

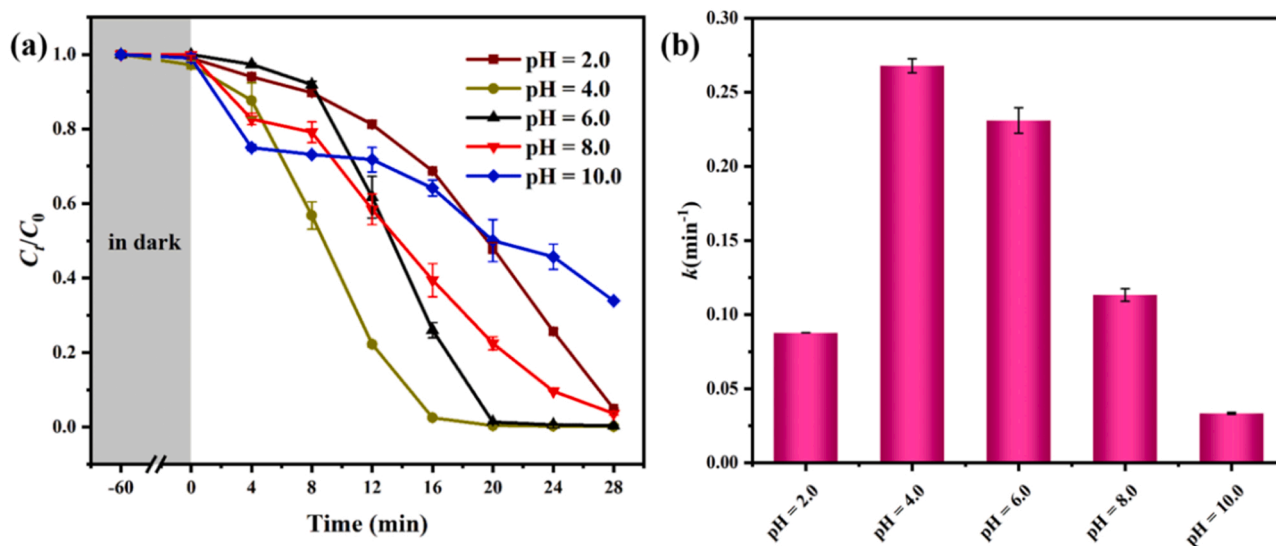


Fig. 7. (a) Influence of different initial pH values on removal of ENR, (b) the corresponding  $k$  values, condition: ENR = 10 mg/L, catalyst = 0.4 g/L,  $H_2O_2$  = 3.0 mM.



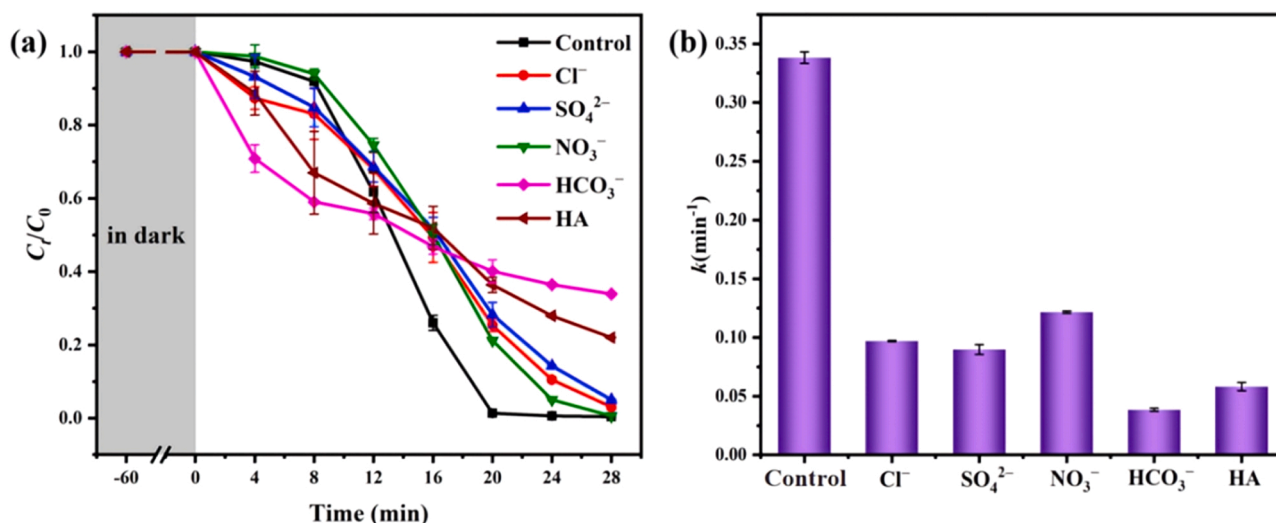


Fig. 8. (a) Influence of inorganic anions and DOM on the ENR degradation over the M3B7/Vis/ $\text{H}_2\text{O}_2$  system, (b) the corresponding degree of  $k$  values. Condition: ENR = 10 mg/L, M3B7 = 0.4 g/L,  $\text{H}_2\text{O}_2$  = 3.0 mM, anions = 1.0 mM.

$0.115 \pm 0.00861$  to  $0.367 \pm 0.01916 \text{ min}^{-1}$  (Fig. 6b). This result should be ascribed to the higher concentration of  $\text{H}_2\text{O}_2$  favored to the production of ROSs and counteracted the charge carriers recombination of the M3B7 during ENR decomposition process. But with further rising the  $\text{H}_2\text{O}_2$  concentration to 5.0 mM, the catalytic degradation rate was somewhat decreased to  $0.363 \pm 0.00689 \text{ min}^{-1}$ . The above results can be ascribed to the disadvantageous self-scavenging of  $\bullet\text{OH}$  and the conversion of  $\bullet\text{OH}$  into  $\text{H}_2\text{O}$ , as described in Eqs. 3-4 [47]. Based on the above results, 3.0 mM of  $\text{H}_2\text{O}_2$  was the optimum concentration and used for subsequent experiments.



### 3.2.2. Effect of initial pH

The pH of solution has remarkable effects on the surface electrical behavior, catalyst's stability, existing forms of reactive species and their redox potentials [48]. Therefore, the effect of initial pH on the ENR removal over the M3B7/Vis/ $\text{H}_2\text{O}_2$  system was studied. As shown in Fig. 7a, the total removal efficiencies exhibited negligible differences when the initial pH increasing from 2.0 to 8.0, reaching approximately 100 % of ENR molecules were degraded within 28 min of visible light irradiation. Furthermore, it revealed that the maximum kinetic constant ( $0.268 \pm 0.00478 \text{ min}^{-1}$ ) was achieved when the pH value being 4.0, as illustrated in Fig. 7b. This was likely because a lower pH can facilitate the activation of ferric species in the photo-Fenton-like system [49]. However, under highly acidic condition like pH = 2.0, proton-promoted dissolution led to partial skeletal collapse of MIL-88A(Fe), thereby the total catalytic efficiency was bound to decrease [50]. Moreover, under alkaline condition (pH = 10.0), the ENR removal efficiency decreased to 66.1 % with reaction rate being  $0.033 \pm 0.00054 \text{ min}^{-1}$ . This experimental phenomenon may presumably be an outcome of two reasons. Firstly, in an alkaline atmosphere,  $\text{H}_2\text{O}_2$  readily broke down into  $\text{O}_2$  and  $\text{H}_2\text{O}$ , which reduced the generation of ROSs (Eq. 5). [51]. Secondly, in alkaline conditions, Fe-MOFs rapidly generate inactive iron-based ions and oxyhydroxide precipitates (Eq. 6) [52], which was inclined to impede the  $\text{Fe}^{3+}/\text{Fe}^{2+}$  transition. Additionally, as pH steadily increased, more  $\text{OH}^-$  occupied the  $\text{Fe}^{3+}$  sites, thereby blocking the interaction between  $\text{Fe}^{3+}$  and  $\text{H}_2\text{O}_2$  and lowering the rate of catalytic degradation. Considering that most real wastewaters environments demonstrate near-neutral pH, the optimum pH of the M3B7/Vis/ $\text{H}_2\text{O}_2$  system was

selected as 6.0. More importantly, the feasibility of working at near-neutral pH might supply an opportunity to utilize the constructed photo-Fenton-like system in practical applications.



### 3.2.3. Effect of co-existing matters

The heterogeneous photo-Fenton-like performance might be impacted by dissolved organic matter (DOM) and other inorganic ions in real-world wastewater in a variety of ways, including by modifying pH, capturing free radicals, and interfering with the breakdown of  $\text{H}_2\text{O}_2$  [53]. As depicted in Fig. 8a, the ENR removal efficiency was only 69.4 % in the presence of 1.0 mM of  $\text{HCO}_3^-$ . This result demonstrated that  $\text{HCO}_3^-$  acted as a scavenger to trap  $\bullet\text{OH}$  (as expressed in Eq. 7) [54] and increased the solution pH to an alkaline condition, which adversely influenced the catalytic degradation of ENR. As to the other inorganic anions ( $\text{Cl}^-$ ,  $\text{SO}_4^{2-}$ ,  $\text{NO}_3^-$ ), they had almost no effect on the total removal efficiency of ENR, but the corresponding reaction rates were significantly reduced to  $0.0967 \pm 0.00004$ ,  $0.0839 \pm 0.00051$  and  $0.1246 \pm 0.00003 \text{ min}^{-1}$ , respectively (Fig. 8b). For the co-existence of  $\text{Cl}^-$ , the inhibitory effect was primarily on account of the  $\bullet\text{OH}$ -scavenging role and production of weaker radicals, such as  $\text{ClOH}\bullet^-$ ,  $\text{Cl}\bullet$  and  $\text{Cl}_2\bullet^-$  (Eqs. 8–12) [55]. Our previous reports [22] had suggested that the N atoms in the piperazinyl structure of FQs might be oxidized by the  $\bullet\text{OH}$  radicals for generating  $\text{NO}_3^-$  anions. According to the Le Chatelier's principle, the production of  $\text{NO}_3^-$  weakened the ENR oxidation process. And the lower catalytic degradation rate with addition of 1.0 mM of  $\text{SO}_4^{2-}$  should be attributed to the generated  $\text{SO}_4\bullet^-$  (Eq. 13) had higher selectivity for target organic pollutants as compared to  $\bullet\text{OH}$  radicals [56].

DOM is present in most treated wastewater at a concentration of 5–30 mg/L and in surface water at a concentration of 1–10 mg/L [57]. According to earlier research, DOM can scavenge radicals and prevent light from penetrating during some photo-Fenton-like processes [58], which reduced the efficiency of these processes for pollutant transformation. Humic acid (HA) was added to the mixture in this investigation, and it did have a slight inhibitory impact, but the ENR degradation efficiency remained at 79.1 % (Fig. 8a). The following explanations should be given for this phenomenon. First, according to Eqs. 14–15, DOM in the excited triplet state was prone to facilitate the photodegradation of organic contaminants by producing singlet oxygen

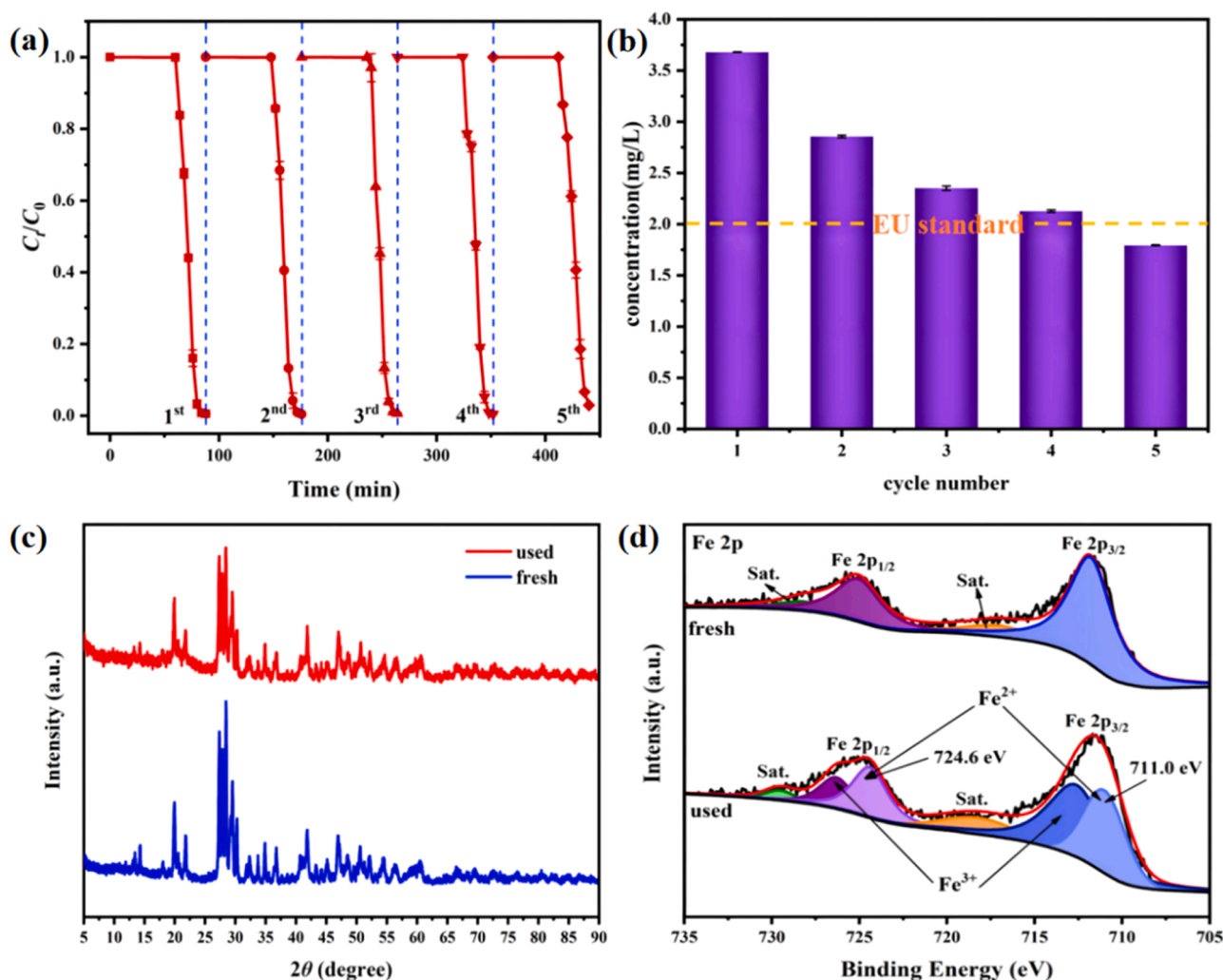


Fig. 9. (a) Cycling experiments of ENR degradation in the M3B7/Vis/ $H_2O_2$  system under the optimum condition, (b) Fe leaching concentration after each cycle, (c) PXRD patterns and Fe 2p XPS spectra before and after catalytic degradation process.

when exposed to light [59]. Secondly, the reaction occurred between  $\bullet OH$  and DOM can generate DOM radicals ( $DOM\bullet$ ), which may also contribute to the degradation of ENR during photo-Fenton-like process (Eq. 16) [57]. Finally, DOM usually contains a variety of active groups, such as carboxyl and carbonyl groups, which typically serve as electron shuttles for improving  $Fe^{3+}/Fe^{2+}$  cycling and  $\bullet OH$  production [60].



### 3.2.4. Evaluation of reusability and stability

To evaluate the potential applications of the M3B7/Vis/ $H_2O_2$  system, the M3B7 was collected by vacuum filtration after reaction, washed with ultrapure water and allowed to dry in an oven at 60 °C overnight to fully eliminate the intermediate products. As illustrated in Fig. 9a, an insignificant reduction of ENR removal can be found after five cycles. Moreover, the Fe leaching concentration of M3B7 heterojunction significantly reduced to 1.79 mg/L (Fig. 9b), which accorded with the environmental standard (2 mg/L) formulated by the European Union [61]. Additionally, the PXRD pattern and SEM micrograph of M3B7 obtained after the fifth run were exhibited in Fig. 9c and Fig. S2. It could be found that no obvious changes in its phase structure and morphology, confirming that the framework of the M3B7 heterojunction was preserved. More importantly, Fig. 9d displayed high-resolution Fe 2p XPS spectra of the fresh and used M3B7 samples. The fresh sample exhibited the typical peaks at 725.2 eV ( $Fe^{3+}$ ) and 712.0 eV ( $Fe^{3+}$ ), which can be attributed to the  $Fe^{3+}$  species existed in the fresh M3B7 heterojunction. After the fifth run of catalytic reaction, the corresponding binding energies were shifted to lower locations at 724.6 eV and 711.0 eV, respectively, which demonstrated the presence of  $Fe^{2+}$  species in the used M3B7 heterojunction, giving evidence for the cycling between  $Fe^{3+}/Fe^{2+}$  pairs [23]. In all, the above experimental phenomena revealed that the as-prepared M3B7 had good stability and can be a good candidate as photo-Fenton catalyst for the treatment of refractory contaminants.

**Table 1**

The cost of ENR degradation using different reaction systems based on  $EE/O$  concept.

System	$EE/O$ (kW•h/m <sup>3</sup> )			Cost (USD/m <sup>3</sup> )
	$EE/O_{Vis}$	$EE/O_{Oxidant}$	$EE/O_{total}$	
MIL-88A(Fe)/Vis/H <sub>2</sub> O <sub>2</sub>	0.073	19.42	19.493	1.3645
BOHP/Vis/H <sub>2</sub> O <sub>2</sub>	0.622	164.4	165.022	11.5515
M3B7/Vis/H <sub>2</sub> O <sub>2</sub>	0.0031	0.822	0.8521	0.0596

### 3.2.5. Economic applicability of the M3B7/Vis/H<sub>2</sub>O<sub>2</sub> reaction system

The International Union of Pure and Applied Chemistry's (IUPAC)  $EE/O$  (electrical energy per order) concept was utilized to complete the cost estimation in an attempt to further investigate the economic applicability of the various reaction systems (The calculation details were illustrated in ESI Text S7 (Part I)). The amount of electrical energy (kW•h) necessary to break down contaminants in 1 m<sup>3</sup> of polluted water is  $EE/O$  [62]. In this investigation, the total electrical energy used ( $EE/O_{total}$ ) was made up of the electrical energy used to illuminate objects with visible light ( $EE/O_{Vis}$ ) and the electrical energy used to produce H<sub>2</sub>O<sub>2</sub> ( $EE/O_{Oxidant}$ ).

Typically, high  $EE/O_{total}$  value represents low energy utilization efficiency. As shown in Table 1, the  $EE/O_{total}$  for ENR removal followed the order of M3B7/Vis/H<sub>2</sub>O<sub>2</sub> (0.8521 kW•h/m<sup>3</sup>) < MIL-88A(Fe)/Vis/H<sub>2</sub>O<sub>2</sub> (19.493 kW•h/m<sup>3</sup>) < BOHP/Vis/H<sub>2</sub>O<sub>2</sub> (165.022 kW•h/m<sup>3</sup>), indicating that the M3B7/Vis/H<sub>2</sub>O<sub>2</sub> system possessed strongest sensibility to visible light and highest utilization efficiency of H<sub>2</sub>O<sub>2</sub> for

degrading ENR molecules. Moreover, assuming that the cost of electricity published by State Grid Corporation of China was 0.07 USD/kW•h, the final  $EE/O$  cost of M3B7/Vis/H<sub>2</sub>O<sub>2</sub> system was calculated to be 0.0596 USD/m<sup>3</sup>, which was much lower than the other reported photo-Fenton systems [63–65]. Additionally, in order to fully estimate the cost of M3B7/Vis/H<sub>2</sub>O<sub>2</sub> system, the expenditures of catalyst fabrication and recovery were also evaluated. The results were exhibited and discussed in ESI Text S7 (Part II).

### 3.2.6. Environmental impacts of the M3B7/Vis/H<sub>2</sub>O<sub>2</sub> reaction system

The application potential of a system should not be evaluated solely based on degradation efficiency of target pollutants, but also need to focus on the discharge of waste, quantification of consumptions, evaluation of emissions and the effects on human health [65]. Therefore, the environmental impacts of M3B7/Vis/H<sub>2</sub>O<sub>2</sub> system were evaluated via LCA, which was a useful tool to predict environmental impacts caused by wastewater treatment technologies. The details of LCA analysis were presented in Text S8.

ReCiPe method was used to evaluate environmental impacts. This method links mid-point and end-point categories [66]. As depicted in Fig. 10a, M3B7/Vis/H<sub>2</sub>O<sub>2</sub> system possessed minima in all indicators compared with BOHP/Vis/H<sub>2</sub>O<sub>2</sub> and M3B7/Vis/H<sub>2</sub>O<sub>2</sub> due to the high efficiency and reaction rate for ENR degradation, suggesting that M3B7/Vis/H<sub>2</sub>O<sub>2</sub> system exerted a minimal impact on the environment. Subsequently, environmental impacts regarding the different stages of the studied processes were investigated. As illustrated in Fig. 10b–d, the stage of catalyst preparation exhibited the maximum value to all

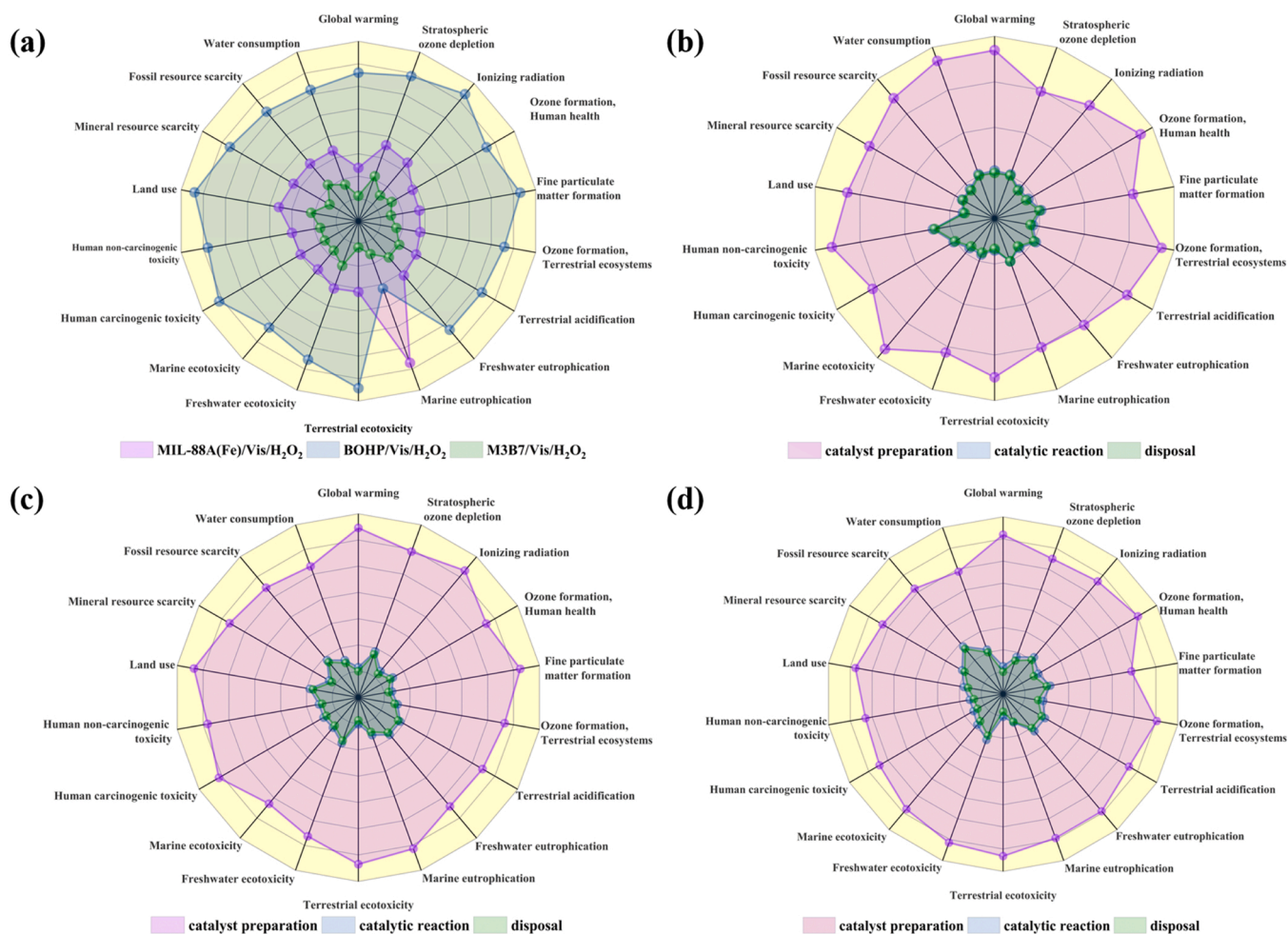


**Fig. 10.** Mid-point environmental impacts in the life cycle of (a) different photo-Fenton systems, and different stages of (b) MIL-88A(Fe)/Vis/H<sub>2</sub>O<sub>2</sub>, (c) BOHP/Vis/H<sub>2</sub>O<sub>2</sub> and (d) M3B7/Vis/H<sub>2</sub>O<sub>2</sub>.



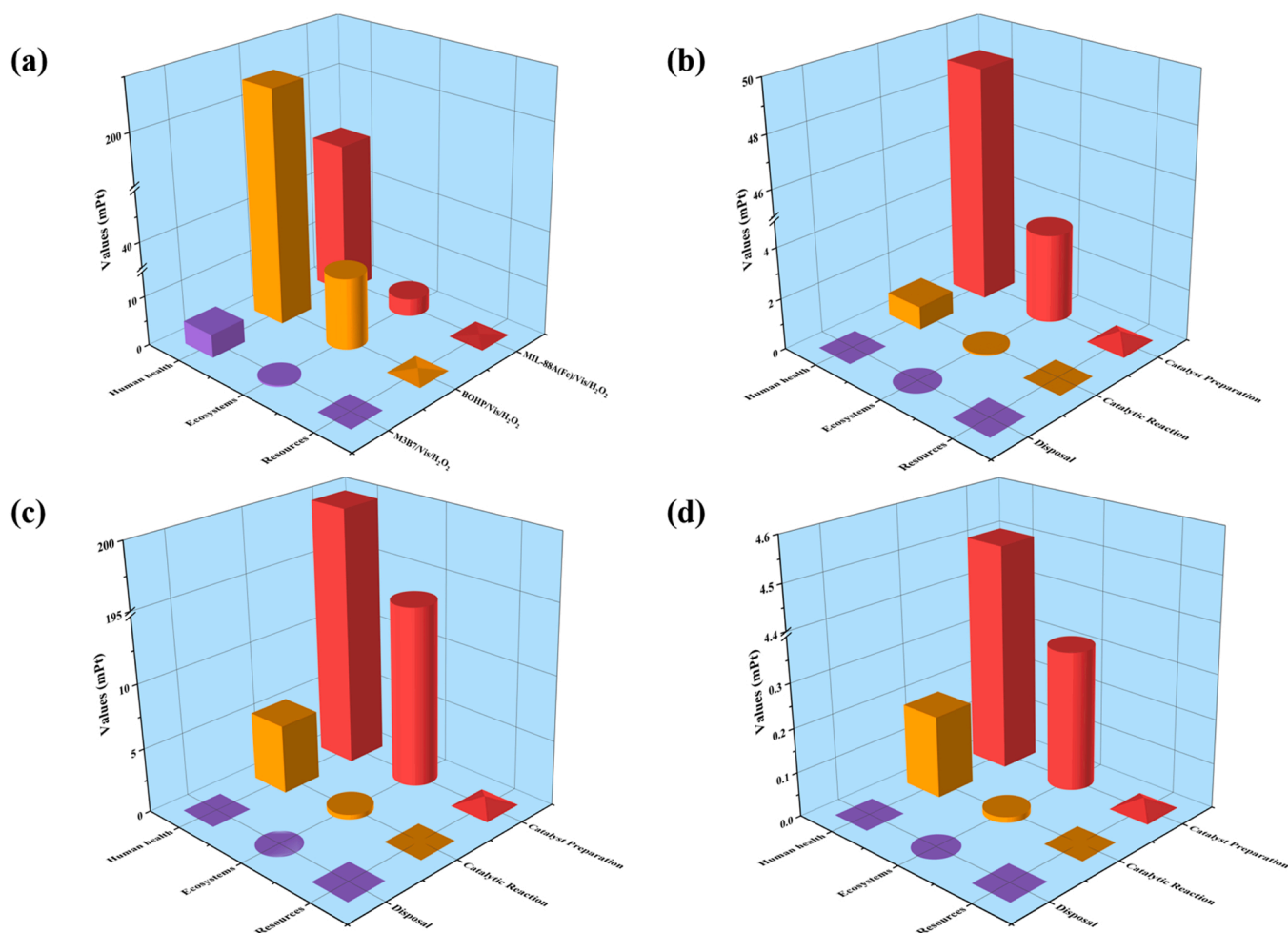


**Fig. 11.** End-point environmental impacts in the life cycle of (a) different photo-Fenton systems, different stages in (b) MIL-88A(Fe)/Vis/H<sub>2</sub>O<sub>2</sub>, (c) BOHP/Vis/H<sub>2</sub>O<sub>2</sub> and (d) M3B7/Vis/H<sub>2</sub>O<sub>2</sub> systems.

categories impact, which could be attributed to the consumption of electric energy and chemical reagents.

To further investigate the impacts for environment, the mid-point was transformed into end-point impact through normalization and weighting processes. As depicted in Fig. 11a, it was obvious that M3B7/Vis/H<sub>2</sub>O<sub>2</sub> caused the lowest environmental impact, which was ascribed to its higher catalytic reactivity as aforementioned. Regarding to impacts of different stages, it could be concluded from Fig. 11b-d that the stage of catalyst preparation possessed the highest value of environmental impact, which was mainly due to the input of chemical reagents and electric energy. As a whole, the above LCA analyses demonstrated that M3B7/Vis/H<sub>2</sub>O<sub>2</sub> displayed reactively great applied potential due to its lower impact caused by removal of ENR per unit mass. Additionally, the higher impact of catalyst preparation stage implied that the practical value of heterogenous photo-Fenton technology could be improved to a certain extent via reducing the consumption of electric energy and chemical reagents. In our future study, MIL-88A(Fe) will be synthesized at room temperature to reduce the consumption of electric energy [24]. Meanwhile, the DMF can be replaced by eco-friendly solvents like ethanol or even water to reduce the impact of waste liquid. As to BOHP, some attempts can be devoted to developing alternative preparation methods with less reaction time to save electricity. Moreover, some methods with low energy consumption during fabrication of MxBy heterojunctions will be tapped to further lower the environmental impact.

### 3.3. Catalytic mechanism

The migration and separation of electron-hole pairs in different catalysts were demonstrated by combining the analysis of photoluminescence spectra (PL), time resolved PL spectra (TRPL), transient photocurrent response and electrochemical impedance spectra (EIS). According to Fig. 12a, the fabrication of heterojunctions between MIL-88A(Fe) and BOHP could successfully inhibit the potential recombination of photo-generated charge carriers since the PL intensities radiated by the MxBy heterojunctions were less in comparison to those of MIL-88A(Fe) and BOHP. As to the MxBy heterojunctions, their PL emission intensities followed in the order of M9B1 > M7B3 > M1B9 > M5B5 > M3B7, indicating that the M3B7 exhibited best photoelectrochemical performance than the other MxBy heterojunctions. And it may cause more electrons participated in the photo-Fenton-like reaction. Subsequently, TRPL was conducted to estimate the quantum lifetime of photo-generated charge carriers [67]. As depicted in Fig. 12b, the average fluorescence lifetime ( $\tau_{\text{average}}$ ) of M3B7 increased to 4.80 ns in comparison to 2.84 ns of MIL-88A(Fe) and 1.42 ns of BOHP. The phenomenon was mainly related to the spatial separation of photo-active electrons at the interface between BOHP and MIL-88A(Fe), corroborating well with the PL results. Additionally, when compared to BOHP and MIL-88A(Fe) in their pristine forms, the M3B7 had the highest transient photocurrent response density (Fig. 12c), also suggesting that more electrons were generated during the photo-excitation process [68].

The electrical conductivity of the as-prepared catalysts was then ascertained using EIS analysis. In most cases, the matching EIS arc radius



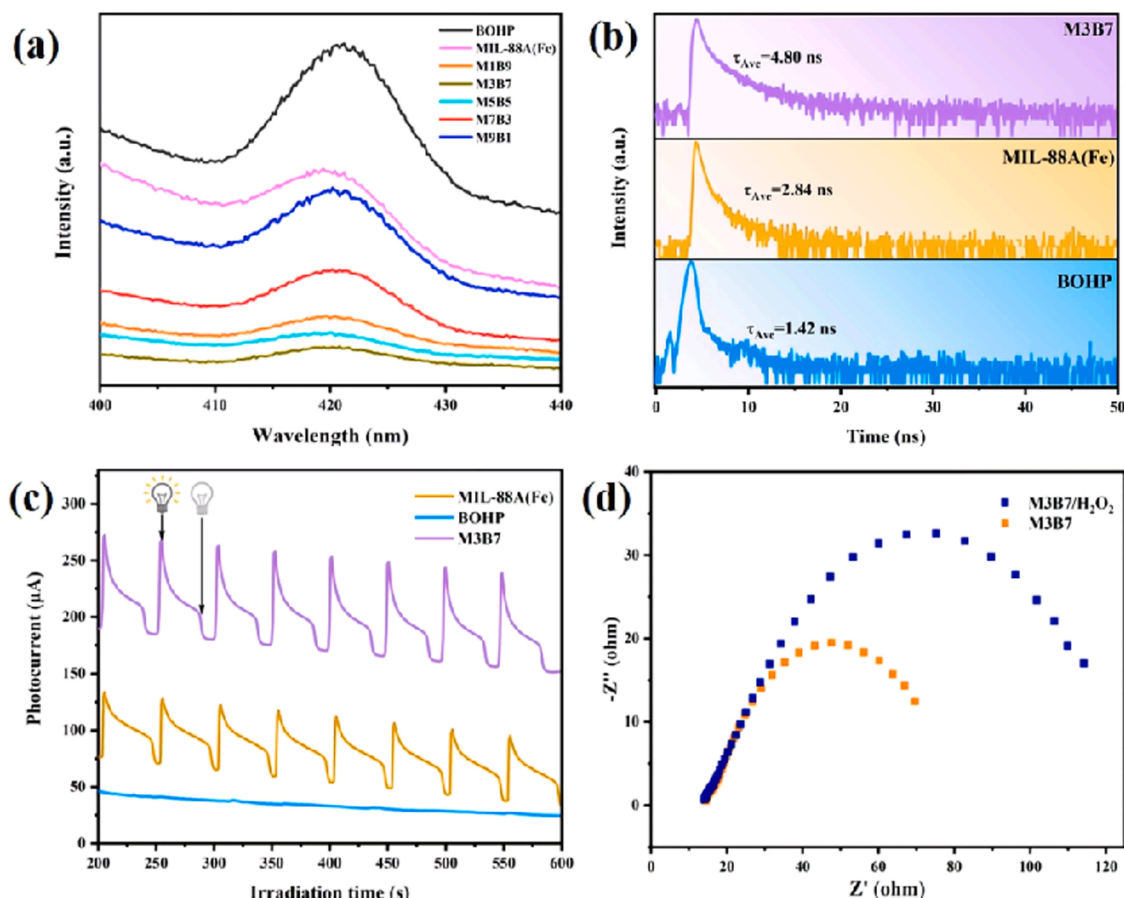


**Fig. 12.** (a) Steady-state PL spectra of the different catalysts, (b) time-resolved PL decay spectra and (c) transient photocurrent response densities of the MIL-88A(Fe), BOHP and M3B7, (d) EIS Nyquist plots of the M3B7 with and without  $H_2O_2$ .

represents the surface charge transfer resistance of the catalyst. As seen in Fig. S3, the M3B7 heterojunction had a smaller semicircular arc radius than MIL-88A(Fe) and BOHP, which was consistent with the increased charge transfer efficiency demonstrated by the PL, TRPL, and transient photocurrent response studies. More importantly, it can be found that a smaller charge transfer resistance was detected in the absence of  $H_2O_2$ , which was attributed to the consumption of electrons during the photo-Fenton-like process (Fig. 12d) [69].

Density functional theory (DFT)-based first-principle calculations were carried out to fully comprehend the interfacial electron transfer mechanism. As shown in Fig. S4a, the metal cluster of MIL-88A(Fe) was coupled with the  $(-2 \times 2 \times 1)$  lattice plane of the BOHP slab to mimic the structural model of the MxBy heterojunction. Firstly, the bonding relationship between the MIL-88A(Fe) and BOHP was revealed using the electronic location function (ELF). The position-dependent function ELF has a range of 0–1. In regions close to 1, strong covalent bonded electrons or lone-pair electrons are present whereas a homogeneous electron gas is present in regions close to 0.5, and extremely low electron densities are usual in regions near 0. [68]. As shown in Fig. 13a, the large ELF values of O and P atoms in the structural model unambiguously unmasked the presence of stable Fe–O–P covalent bonds (length ca 0.1917 Å) between O atoms from MIL-88A(Fe) and P atoms from BOHP, which was consistent with the XPS investigation. It was important to note that the atomic-level charge flow highway was conducive to accelerate electron flow between the two components, thereby boosting the activation activity of  $H_2O_2$  when exposed to visible light. After that, work function results were acquired through electrostatic potential analysis to analyze band alignment and free electron transfer of MxBy heterojunctions. As depicted in Fig. 13b–c, the work function of MIL-88A(Fe) was computed to be 4.84 eV, which was somewhat less than the  $(-2$

2 1) surface of BOHP (5.03 eV). Thereby, the free electrons in MIL-88A(Fe) surface with a high  $E_F$  ( $-4.84$  eV) might undergo spontaneous diffusion into the BOHP surface with a low  $E_F$  ( $-5.03$  eV) via the formed Fe–O–P bond. Additionally, the difference charge density (Fig. S4b) further confirmed the interfacial charge distribution, wherein the density of the electron cloud of BOHP accumulated on the O and P atoms while being depleted on the Fe atoms of MIL-88A(Fe). The potential energies of MxBy heterojunction with and without the Fe–O–P link were computed in order to acquire a thorough understanding of the function of the interfacial chemical bond in the event of charge transfer. The electron transfer from MIL-88A(Fe) to BOHP required overcoming an energy barrier of 59.41 eV, and the transfer distance was 3.104 Å when MIL-88A(Fe) and BOHP interacted with van der Waals force (Fig. 13d). However, by generating an interfacial Fe–O–P chemical connection, the transfer distance and energy barrier can be respectively reduced to 1.917 Å and 26.69 eV (Fig. 13e). The aforementioned findings showed that the electron transfer through the Fe–O–P bond was more energetically favorable. As a result, the interfacial Fe–O–P bond can effectively increase the catalytic efficiency via simultaneously lowering the migration distance and energy barrier of charge transfer inside heterojunction.

Except for the electron transfer mechanism, it is generally known that the main reactive species play the decisive role in the photo-Fenton-like degradation reaction, so the radical trapping experiments with different scavengers were conducted in this research. As illustrated in Fig. S5, three quenching agents, triethanolamine (TEA, 50 mmol/L,  $h^+$  scavenger),  $N_2$  atmosphere ( $\bullet O_2^-$  scavenger) and tert-butyl alcohol (TBA, 50 mmol/L,  $\bullet OH$  scavenger) were chosen to determine the active species in the M3B7/Vis/ $H_2O_2$  reaction system [70]. It was obvious that ENR degradation efficiencies were restrained by addition of TBA (24.6 %)

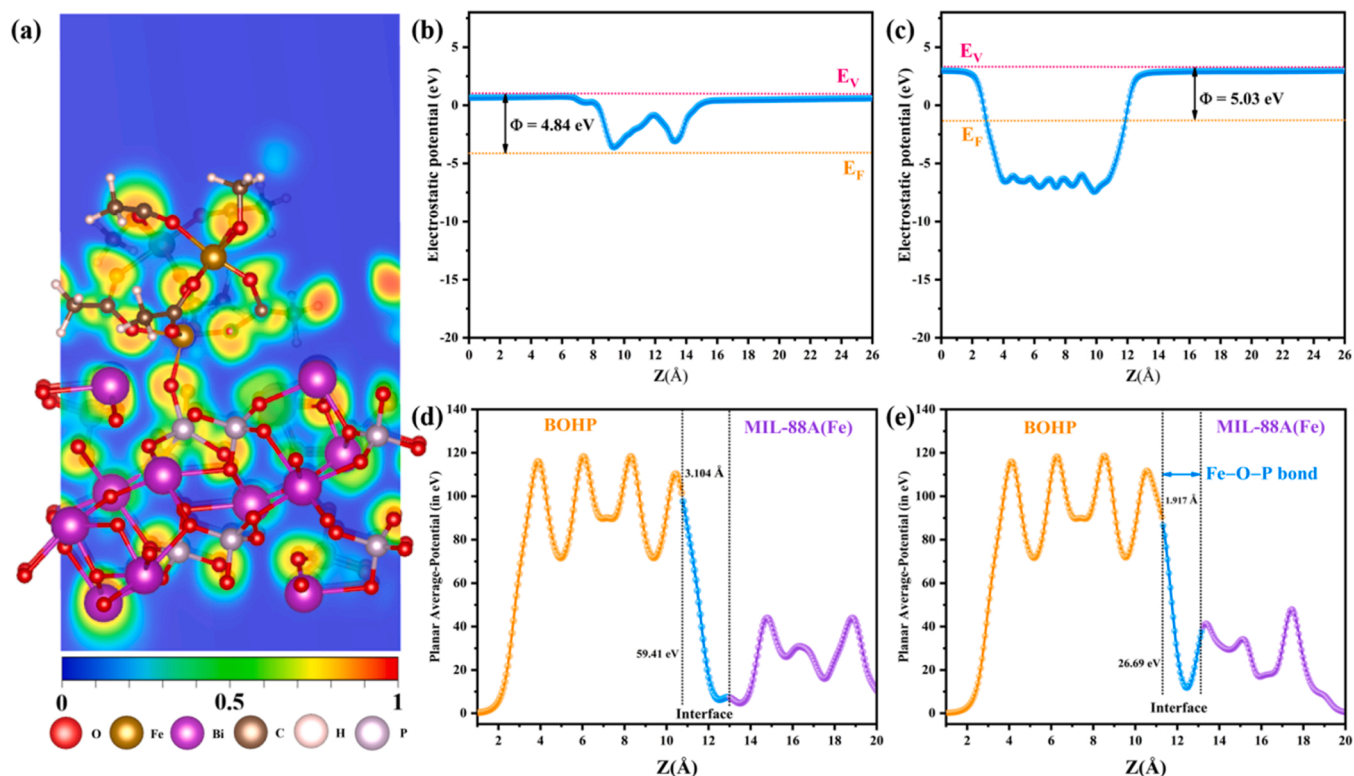


Fig. 13. (a) 2D electronic location function of the interlayer, electrostatic potential of (b) MIL-88A(Fe) and (c) BOHP, potential energies of MIL-88A(Fe)/BOHP (d) without and with (e) of Fe–O–P bond.

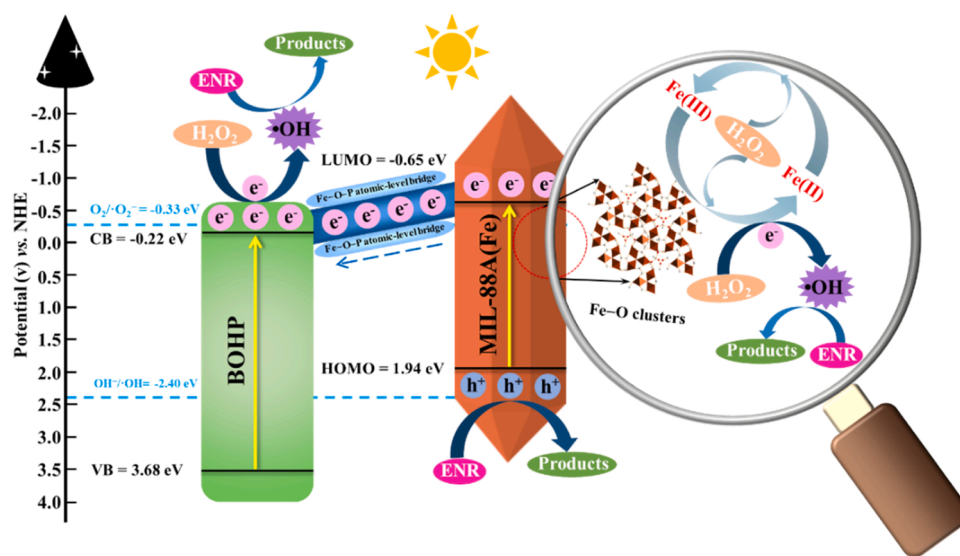


Fig. 14. Possible ENR catalytic degradation mechanism over the M3B7/Vis/ $\text{H}_2\text{O}_2$  system.

and TEA (5.8 %), revealing that  $\bullet\text{OH}$  and  $\text{h}^+$  were the dominant oxidizing substances. ESR was additionally used to validate the production of  $\bullet\text{OH}$  across several catalytic systems [71]. As shown in Fig. S6a-c, faint  $\bullet\text{OH}$  signal was seen under the dark condition, but the quartet signal of DMPO- $\bullet\text{OH}$  was clearly recorded upon the visible light irradiation in the spectra of MIL-88A(Fe)/Vis/ $\text{H}_2\text{O}_2$  and M3B7/Vis/ $\text{H}_2\text{O}_2$  systems, verifying  $\bullet\text{OH}$  might generate by activating  $\text{H}_2\text{O}_2$  over Fe–O clusters or photo-generated electrons transfer. This result further declared that  $\bullet\text{OH}$  was the predominant ROS during the photocatalytic-Fenton-like process.

Additionally, the Mott–Schottky measurements of MIL-88A(Fe) and

BOHP were also conducted to determine their flat band potentials ( $E_{\text{fb}}$ ). As shown in Fig. S7a-b, the  $E_{\text{fb}}$  of MIL-88A(Fe) and BOHP were fitted respectively as  $-0.75$  eV and  $-0.32$  eV vs. Ag/AgCl electrode. The slopes of  $C^{-2}$  value versus potential were positive, demonstrating that MIL-88A(Fe) and BOHP were both the n-type semiconductors [72]. As to the majority of n-type semiconductors, the  $E_{\text{fb}}$  is more positive 0.1 eV than the conduction band potential ( $E_{\text{CB}}$ ) [73]. Therefore, the lowest unoccupied molecular orbital potential ( $E_{\text{LUMO}}$ ) of MIL-88A(Fe) and conduction band potential ( $E_{\text{CB}}$ ) of BOHP were  $-0.65$  eV and  $-0.22$  eV vs. NHE, respectively, which matched well with the previous reports [21,23]. Therefore, the highest occupied molecular orbital

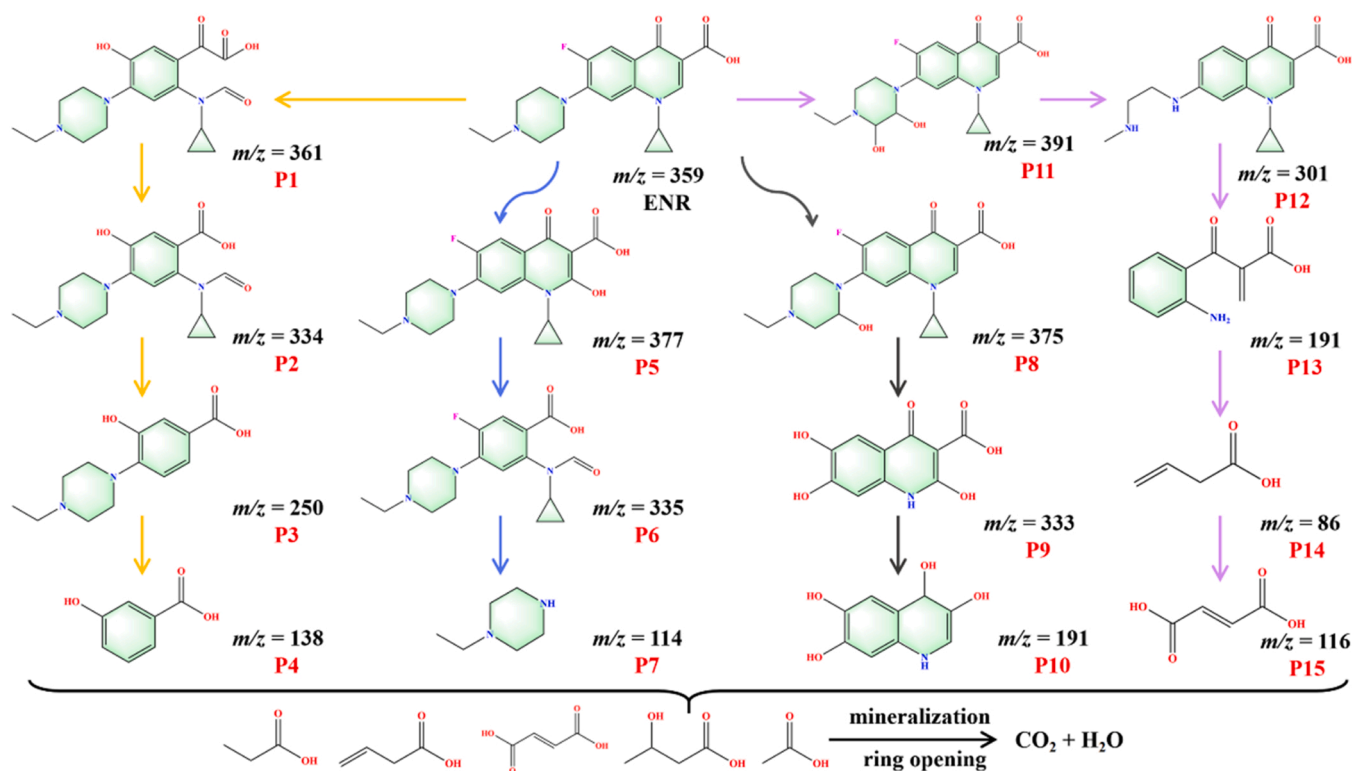
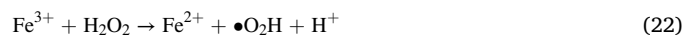
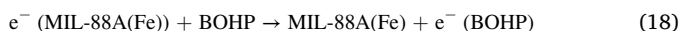


Fig. 15. Proposed ENR degradation pathways over the M3B7/Vis/H<sub>2</sub>O<sub>2</sub> reaction system.

potential ( $E_{\text{HOMO}}$ ) of MIL-88A(Fe) and valence band potential ( $E_{\text{VB}}$ ) of BOHP were computed to be 1.94 eV and 3.68 eV vs. NHE based on the estimated band gaps, respectively.

Based on the above discussion, a conceivable catalytic mechanism was proposed in Fig. 14 with visible light irradiation, photo-generated holes and electrons were activated and gathered on HOMO and LUMO of MIL-88A(Fe). However, BOHP was not excited by visible light due to the wide band gap (3.90 eV) (Eqs. 17–18). Subsequently, the electrons in LUMO of MIL-88A(Fe) were inclined to thermodynamically migrate to the CB of BOHP due to its more negative CB than MIL-88A(Fe), leaving the holes on the HOMO of MIL-88A(Fe), thus the separation rate of charge carriers would be dramatically improved within MIL-88A(Fe) and BOHP. The Fe–O–P bond acting as atomic-level interfacial “bridge” could enhance the photo-generated electrons migration from MIL-88A(Fe) to BOHP, thus dramatically accelerating the transfer of photo-generated electrons. Additionally, H<sub>2</sub>O<sub>2</sub> photolysis occurred under visible light and then induced the production of •OH (Eqs. 19–20). In view of the constructed reaction system belonged to heterogeneous Fenton-like process, hence the photo-generated electrons could effectively accelerate the transformation from Fe<sup>3+</sup> to Fe<sup>2+</sup>, and the Fe<sup>3+</sup>/Fe<sup>2+</sup> redox cycle was favorable to the formation of more •OH through the addition of H<sub>2</sub>O<sub>2</sub> (Eqs. 21–23). Summarily, the generated •OH and h<sup>+</sup> with considerable oxidative capability could effectively removal ENR. More importantly, the synergism between heterogeneous Fenton-like reaction and photocatalysis could be attributed to suitable band alignment and the formed Fe–O–P bond acted as an atomic-level channel for promotion of electron transfer.



### 3.4. ENR degradation pathways and ecotoxicity analysis

LC-MS/MS technique was employed to confirm the intermediates of ENR generated in the constructed reaction system. Furthermore, the probable degradation pathways were speculated. As illustrated in Fig. 15, it can be conjectured that four ENR degradation pathways might occur in M3B7/Vis/H<sub>2</sub>O<sub>2</sub> catalytic degradation system.

**Pathway I:** The route originates from the defluorination process. The F atom of ENR molecule was replaced by –OH through •OH addition while the C=C bond in the pyridine ring underwent cleavage by the h<sup>+</sup> attack, which induced the generation of P1. Subsequently, P1 was decarboxylated to generate P2 under h<sup>+</sup> attack. The P2 would be further oxidized by h<sup>+</sup> through C–N bond cleavage reaction and formed P3. Ultimately, the cleavage of C–N bond between the piperazine ring and benzene ring provoked the production of P4.

**Pathway II:** The key location of this route was the quinolone ring. The quinolone ring was initially attacked by •OH to create the hydroxylated products (P5). These products were then further oxidized by h<sup>+</sup>, causing the ring to cleave and the creation of the intermediate intermediates (P6). P6 would eventually produce P7 after being further oxidized by h<sup>+</sup> through bond cleavage events.

**Pathway III:** This route was mainly the loss of the piperazine ring and cyclopropyl group. First of all, hydroxylation process took place on the piperazine ring and formed P8. Subsequently, P9 was generated after continuous ring cleavage reactions driven by •OH and h<sup>+</sup>. Additionally, the quinolone ring's carboxyl group is a potent electron-withdrawing group that •OH may readily attack and cause dihydroxylation reaction [74]. As a result, P10 was formed after the hydroxylation and decarboxylation process.

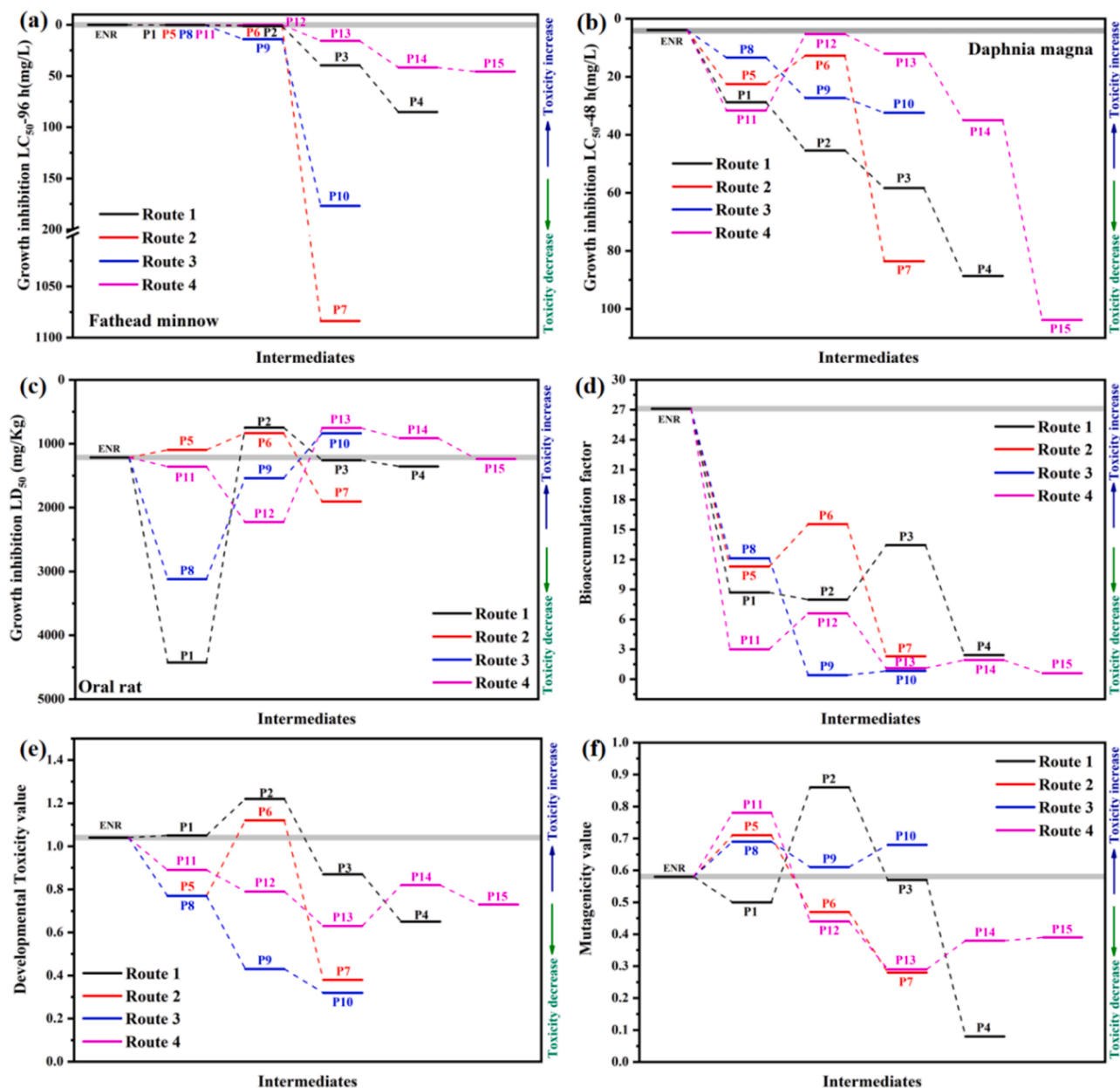


Fig. 16. (a) Fathead minnow  $LC_{50}$  (96 h), (b) *Daphnia magna*  $LC_{50}$  (48 h), (c) oral rat  $LD_{50}$ , (d) bioaccumulation factor, (e) developmental toxicity and (f) mutagenicity of ENR and its degradation intermediates.

Pathway IV: This pathway included the destruction of carboxyl group and the ring-opening process of piperazine ring. Specifically, hydroxylation reaction took place on piperazine ring and generated P11, and then the piperazine ring was completely destroyed to form P12 in the presence of  $h^+$  and  $\bullet OH$ . Moreover, the cleavage of C–N bond in pyridine ring and loss of cyclopropyl group induced to the formation of P13. Ultimately, benzene ring cleavage and consecutive chemical bonds breaking resulted in generation of P14 and P15.

The acute toxicity (Fathead minnow, *Daphnia magna*, and Oral rat), developmental toxicity, bioaccumulation factor, and mutagenicity of ENR and its intermediate degradation products were assessed by employing Toxicity Estimation Software Tool (T.E.S.T.) based on QSAR prediction [75]. As shown in Fig. 16, most ultimate intermediates of the proposed four degradation pathways exhibited relatively lower toxicities than ENR except product P10 of pathway III in the aspects of Oral rat  $LD_{50}$  and mutagenicity, suggesting that M3B7/Vis/ $H_2O_2$  was a green and environmentally friendly reaction system.

#### 4. Conclusions

To sum up, a MIL-88A(Fe)/BOHP heterojunction was synthesized via ball-mingling method, which was applied to efficient degradation of ENR through photo-Fenton-like catalysis process. XPS analysis and DFT calculation offered the proofs that interfacial Fe–O–P bond acted as an atomic-level channel for accelerating electron transfer, and decreased the transmission distance and charge transfer energy barrier between MIL-88A(Fe) and BOHP, thereby achieving effective spatial separation of photo-generated electrons. As expected, the optimal reaction system (M3B7/Vis/ $H_2O_2$ ) displayed superior performance for the photo-Fenton removal of ENR, and the catalytic degradation efficiency was close to 100 % within 28 min under visible light. Additionally, the result of toxicity assessment and economy analysis uncovered that M3B7/Vis/ $H_2O_2$  system possessed eco-friendly and energy-efficient properties. A LCA perspective for the M3B7/Vis/ $H_2O_2$ , MIL-88A(Fe)/Vis/ $H_2O_2$ , BOHP/Vis/ $H_2O_2$  systems applied in catalytic degradation of ENR



highlighted that the electric energy and chemical reagents were the main impacts during preparation of catalysts. In the future, we will focus on the optimization of MxBy fabrication process to improve the sustainability of the constructed reaction system. In the domain of Fenton-like treatment technologies, this research will also offer an alternative method for fabricating new MOFs/bismuth-based semiconductor heterojunctions for antibiotic removal.

## CRediT authorship contribution statement

**Tianyu Wang:** Data curation, Investigation, Visualization, Writing - Original draft preparation. **Chen Zhao:** Resources, Validation, Supervision, Writing - review & editing. **Linghui Meng:** Resources, Instrumental. **Yujia Li:** Investigation, Instrumental. **Dawei Wang:** Investigation, Resources. **Chong-Chen Wang:** Conceptualization, Funding acquisition, Supervision, Project administration, Writing - review & editing.

## Declaration of Competing Interest

The authors declare that they have no known competing financial interests or personal relationships that could have appeared to influence the work reported in this paper.

## Data availability

Data will be made available on request.

## Acknowledgments

This work was supported by National Natural Science Foundation of China (22176012), Beijing Natural Science Foundation (8202016), R&D Program of Beijing Municipal Education Commission (KM202310016007), The Fundamental Research Funds for Beijing University of Civil Engineering and Architecture (X20147/X20141/X20135/X20146), Young Elite Scientists Sponsorship Program by BAST (BYESS2023100). Thanks to Dr. Yinan Song for his support in LCA analysis.

## Appendix A. Supporting information

Supplementary data associated with this article can be found in the online version at [doi:10.1016/j.apcatb.2023.122832](https://doi.org/10.1016/j.apcatb.2023.122832).

## References

- [1] M. Sturini, A. Speltini, F. Maraschi, A. Profumo, L. Pretali, E. Fasani, A. Albini, Photochemical degradation of marbofloxacin and enrofloxacin in natural waters, *Environ. Sci. Technol.* 44 (2010) 4564–4569, <https://doi.org/10.1021/es100278n>.
- [2] J. Chakraborty, I. Nath, C. Jabbour, N. Aljammal, S. Song, C.-M. Kao, P. M. Heynderickx, F. Verpoort, Novel rapid room temperature synthesis of conjugated microporous polymer for metal-free photocatalytic degradation of fluoroquinolones, *J. Hazard. Mater.* 398 (2020), 122928, <https://doi.org/10.1016/j.jhazmat.2020.122928>.
- [3] M. Harrabi, D.A. Alexandrino, F. Aloulou, B. Elleuch, B. Liu, Z. Jia, C.M.R. Almeida, A.P. Mucha, M.F. Carvalho, Biodegradation of oxytetracycline and enrofloxacin by autochthonous microbial communities from estuarine sediments, *Sci. Total Environ.* 648 (2019) 962–972, <https://doi.org/10.1016/j.scitotenv.2018.08.193>.
- [4] H. Guo, N. Jiang, H. Wang, N. Lu, K. Shang, J. Li, Y. Wu, Pulsed discharge plasma assisted with graphene-WO<sub>3</sub> nanocomposites for synergistic degradation of antibiotic enrofloxacin in water, *Chem. Eng. J.* 372 (2019) 226–240, <https://doi.org/10.1016/j.cej.2019.04.119>.
- [5] B. Suyamud, J. Lohwacharin, Y. Yang, V.K. Sharma, Antibiotic resistant bacteria and genes in shrimp aquaculture water: Identification and removal by ferrate (VI), *J. Hazard. Mater.* 420 (2021), 126572, <https://doi.org/10.1016/j.jhazmat.2021.126572>.
- [6] W. Liu, H. Zhang, B. Cao, K. Lin, J. Gan, Oxidative removal of bisphenol A using zero valent aluminum–acid system, *Water Res.* 45 (2011) 1872–1878, <https://doi.org/10.1016/j.watres.2010.12.004>.
- [7] Z. Chen, C. Lian, K. Huang, J. Ji, Q. Yan, J. Zhang, M. Xing, “Small amount for multiple times” of H<sub>2</sub>O<sub>2</sub> feeding way in MoS<sub>2</sub>-Fe<sub>x</sub> heterogeneous fenton for enhancing sulfadiazine degradation, *Chin. Chem. Lett.* 33 (2022) 1365–1372, <https://doi.org/10.1016/j.ccl.2021.08.016>.
- [8] F. Mendez-Arriaga, S. Esplugas, J. Gimenez, Degradation of the emerging contaminant ibuprofen in water by photo-Fenton, *Water Res.* 44 (2010) 589–595, <https://doi.org/10.1016/j.watres.2009.07.009>.
- [9] Q. Wu, H. Yang, L. Kang, Z. Gao, F. Ren, Fe-based metal-organic frameworks as Fenton-like catalysts for highly efficient degradation of tetracycline hydrochloride over a wide pH range: acceleration of Fe (II)/Fe (III) cycle under visible light irradiation, *Appl. Catal. B: Environ.* 263 (2020), 118282, <https://doi.org/10.1016/j.apcatb.2019.118282>.
- [10] Z. Fang, Y. Liu, J. Qi, Z.-F. Xu, T. Qi, L. Wang, Establishing a high-speed electron transfer channel via CuS/MIL-Fe heterojunction catalyst for photo-Fenton degradation of acetaminophen, *Appl. Catal. B: Environ.* 320 (2023), 121979, <https://doi.org/10.1016/j.apcatb.2022.121979>.
- [11] C. Zhao, J. Wang, X. Chen, Z. Wang, H. Ji, L. Chen, W. Liu, C.-C. Wang, Bifunctional Bi<sub>12</sub>O<sub>17</sub>Cl<sub>2</sub>/MIL-100 (Fe) composites toward photocatalytic Cr (VI) sequestration and activation of persulfate for bisphenol A degradation, *Sci. Total Environ.* 752 (2021), 141901, <https://doi.org/10.1016/j.scitotenv.2020.141901>.
- [12] F.-X. Wang, C.-C. Wang, X. Du, Y. Li, F. Wang, P. Wang, Efficient removal of emerging organic contaminants via photo-Fenton process over micron-sized Fe-MOF sheet, *Chem. Eng. J.* 429 (2022), 132495, <https://doi.org/10.1016/j.cej.2021.132495>.
- [13] G. Gumilar, J. Henzie, B. Yulianto, A. Patah, N. Nugraha, M. Iqbal, M.A. Amin, M.S. A. Hossain, Y. Yamauchi, Y.V. Kaneti, Performance enhancement strategies for surface plasmon resonance sensors in direct glucose detection using pristine and modified UiO-66: effects of morphology, immobilization technique, and signal amplification, *J. Mater. Chem. A* 10 (2022) 6662–6678, <https://doi.org/10.1039/D1TA08741J>.
- [14] C.-H. Wang, D.-W. Zhang, S. Liu, Y. Yamauchi, F.-B. Zhang, Y.V. Kaneti, Ultrathin nanosheet-assembled nickel-based metal-organic framework microflowers for supercapacitor applications, *Chem. Commun.* 58 (2022) 1009–1012, <https://doi.org/10.1039/D1CC04880E>.
- [15] M. Cheng, C. Lai, Y. Liu, G. Zeng, D. Huang, C. Zhang, L. Qin, L. Hu, C. Zhou, W. Xiong, Metal-organic frameworks for highly efficient heterogeneous Fenton-like catalysis, *Coord. Chem. Rev.* 368 (2018) 80–92, <https://doi.org/10.1016/j.ccr.2018.04.012>.
- [16] D. Yu, L. Wang, T. Yang, G. Yang, D. Wang, H. Ni, M. Wu, Tuning Lewis acidity of iron-based metal-organic frameworks for enhanced catalytic ozonation, *Chem. Eng. J.* 404 (2021), 127075, <https://doi.org/10.1016/j.cej.2020.127075>.
- [17] X.-H. Yi, Y. Gao, C.-C. Wang, Y.-H. Li, H.-Y. Chu, P. Wang, Photocatalytic Cr (VI) reduction over MIL-88A (Fe) on polyurethane sponge: From batch to continuous-flow operation, *Chin. Chem. Lett.* (2022), 108029, <https://doi.org/10.1016/j.ccl.2022.108029>.
- [18] Z. Yang, X. Xia, L. Shao, Y. Liu, Efficient photocatalytic degradation of tetracycline under visible light by Z-scheme Ag<sub>3</sub>PO<sub>4</sub>/mixed-valence MIL-88A (Fe) heterojunctions: Mechanism insight, degradation pathways and DFT calculation, *Chem. Eng. J.* 410 (2021), 128454, <https://doi.org/10.1016/j.cej.2021.128454>.
- [19] S. Wang, L. Wang, W. Huang, Bismuth-based photocatalysts for solar energy conversion, *J. Mater. Chem. A* 8 (2020) 24307–24352, <https://doi.org/10.1039/D0TA09729B>.
- [20] C. Zhao, X. Pan, Z. Wang, C.-C. Wang, 1+1>2: a critical review of MOF/bismuth-based semiconductor composites for boosted photocatalysis, *Chem. Eng. J.* 417 (2021), 128022, <https://doi.org/10.1016/j.cej.2020.128022>.
- [21] S.P. Sahu, M. Qanbarzadeh, M. Ateia, H. Torkzadeh, A.S. Maroli, E.L. Cates, Rapid degradation and mineralization of perfluorooctanoic acid by a new petijeanite Bi<sub>3</sub>O(OH)(PO<sub>4</sub>)<sub>2</sub> microparticle ultraviolet photocatalyst, *Environ. Sci. Technol. Lett.* 5 (2018) 533–538, <https://doi.org/10.1021/acs.estlett.8b00395>.
- [22] C. Zhao, Y. Li, H. Chu, X. Pan, L. Ling, P. Wang, H. Fu, C.-C. Wang, Z. Wang, Construction of direct Z-scheme Bi<sub>3</sub>O<sub>7</sub>/UiO-66-NH<sub>2</sub> heterojunction photocatalysts for enhanced degradation of ciprofloxacin: mechanism insight, pathway analysis and toxicity evaluation, *J. Hazard. Mater.* 419 (2021), 126466.
- [23] X.-H. Yi, H. Ji, C.-C. Wang, Y. Li, Y.-H. Li, C. Zhao, A. Wang, H. Fu, P. Wang, X. Zhao, Photocatalysis-activated SR-AOP over PDINH/MIL-88A (Fe) composites for boosted chloroquine phosphate degradation: performance, mechanism, pathway and DFT calculations, *Appl. Catal. B: Environ.* 293 (2021), 120229.
- [24] H. Fu, X.-X. Song, L. Wu, C. Zhao, P. Wang, C.-C. Wang, Room-temperature preparation of MIL-88A as a heterogeneous photo-Fenton catalyst for degradation of rhodamine B and bisphenol A under visible light, *Mater. Res. Bull.* 125 (2020), 110806, <https://doi.org/10.1016/j.materresbull.2020.110806>.
- [25] Y. Zhang, J. Zhou, X. Chen, L. Wang, W. Cai, Coupling of heterogeneous advanced oxidation processes and photocatalysis in efficient degradation of tetracycline hydrochloride by Fe-based MOFs: Synergistic effect and degradation pathway, *Chem. Eng. J.* 369 (2019) 745–757, <https://doi.org/10.1016/j.cej.2019.03.108>.
- [26] J. Cao, X. Li, H. Lin, S. Chen, X.J. John Fu, In situ preparation of novel p-n junction photocatalyst BiOI/(BiO)<sub>2</sub>CO<sub>3</sub> with enhanced visible light photocatalytic activity, *J. Hazard. Mater.* 239 (2012) 316–324, <https://doi.org/10.1016/j.jhazmat.2012.08.078>.
- [27] H. Lin, H. Ye, S. Chen, Y. Chen, One-pot hydrothermal synthesis of BiPO<sub>4</sub>/BiVO<sub>4</sub> with enhanced visible-light photocatalytic activities for methylene blue degradation, *RSC Adv.* 4 (2014) 10968–10974, <https://doi.org/10.1039/C3RA45288C>.
- [28] N. Liu, W. Huang, X. Zhang, L. Tang, L. Wang, Y. Wang, M. Wu, Ultrathin graphene oxide encapsulated in uniform MIL-88A(Fe) for enhanced visible light-driven photodegradation of RhB, *Appl. Catal. B: Environ.* 221 (2018) 119–128, <https://doi.org/10.1016/j.apcatb.2017.09.020>.

- [29] D. Huang, X. Sun, Y. Liu, H. Ji, W. Liu, C.-C. Wang, W. Ma, Z. Cai, A carbon-rich g-C<sub>3</sub>N<sub>4</sub> with promoted charge separation for highly efficient photocatalytic degradation of amoxicillin, *Chin. Chem. Lett.* 32 (2021) 2787–2791, <https://doi.org/10.1016/j.ccllet.2021.01.012>.
- [30] Z. Yang, X. Xu, X. Liang, C. Lei, Y. Wei, P. He, B. Lv, H. Ma, Z. Lei, MIL-53 (Fe)-graphene nanocomposites: efficient visible-light photocatalysts for the selective oxidation of alcohols, *Appl. Catal. B: Environ.* 198 (2016) 112–123, <https://doi.org/10.1016/j.apcatb.2016.05.041>.
- [31] X. Hou, K. Hu, H. Zhang, Z. Tao, M. Yang, G. Wang, Construction of 2D MOFs@reduced graphene oxide nanocomposites with enhanced visible light-induced fenton-like catalytic performance by seeded growth strategy, *ChemCatChem* 11 (2019) 4411–4419, <https://doi.org/10.1002/cctc.201900760>.
- [32] Q. Hao, R. Wang, H. Lu, W. Ao, D. Chen, C. Ma, W. Yao, Y. Zhu, One-pot synthesis of C/Bi<sub>2</sub>O<sub>3</sub> composite with enhanced photocatalytic activity, *Appl. Catal. B: Environ.* 219 (2017) 63–72, <https://doi.org/10.1016/j.apcatb.2017.07.030>.
- [33] L.-J. Meng, C.P.M. de Sá, M. Dos Santos, Study of the structural properties of ZnO thin films by x-ray photoelectron spectroscopy, *Appl. Surf. Sci.* 78 (1994) 57–61, [https://doi.org/10.1016/0169-4332\(94\)90031-0](https://doi.org/10.1016/0169-4332(94)90031-0).
- [34] F. Mei, J. Zhang, K. Dai, G. Zhu, C. Liang, A Z-scheme Bi<sub>2</sub>MoO<sub>6</sub>/CdSe-diethylenetriamine heterojunction for enhancing photocatalytic hydrogen production activity under visible light, *Dalton Trans.* 48 (2019) 1067–1074, <https://doi.org/10.1039/C8DT04578J>.
- [35] S. Guo, S. Wang, N. Wu, J. Liu, Y. Ni, W. Liu, Facile synthesis of porous Fe<sub>2</sub>TiO<sub>5</sub> microparticles serving as anode material with enhanced electrochemical performances, *RSC Adv.* 5 (2015) 103767–103775, <https://doi.org/10.1039/C5RA22930H>.
- [36] Y. Zhang, Y. Ma, L. Wang, Q. Sun, F. Zhang, J. Shi, Facile one-step hydrothermal synthesis of noble-metal-free hetero-structural ternary composites and their application in photocatalytic water purification, *RSC Adv.* 7 (2017) 50701–50712, <https://doi.org/10.1039/C7RA10732C>.
- [37] D. Fa, B. Yu, Y. Miao, Synthesis of ultra-long nanowires of nickel phosphate by a template-free hydrothermal method for electrocatalytic oxidation of glucose, *Colloids Surf. A: Physicochem. Eng. Asp.* 564 (2019) 31–38, <https://doi.org/10.1016/j.colsurfa.2018.12.035>.
- [38] M. Li, T. Liu, X. Bo, M. Zhou, L. Guo, S. Guo, Hybrid carbon nanowire networks with Fe–P bond active site for efficient oxygen/hydrogen-based electrocatalysis, *Nano Energy* 33 (2017) 221–228, <https://doi.org/10.1016/j.nanoen.2017.01.026>.
- [39] R. Shen, L. Zhang, N. Li, Z. Lou, T. Ma, P. Zhang, Y. Li, X. Li, W–N bonds precisely boost Z-scheme interfacial charge transfer in g-C<sub>3</sub>N<sub>4</sub>/WO<sub>3</sub> heterojunctions for enhanced photocatalytic H<sub>2</sub> evolution, *ACS Catal.* 12 (2022) 9994–10003, <https://doi.org/10.1021/acscatal.2c02416>.
- [40] X. Wang, X. Wang, J. Huang, S. Li, A. Meng, Z. Li, Interfacial chemical bond and internal electric field modulated Z-scheme S<sub>2</sub>-ZnIn<sub>2</sub>S<sub>4</sub>/MoSe<sub>2</sub> photocatalyst for efficient hydrogen evolution, *Nat. Commun.* 12 (2021) 4112, <https://doi.org/10.1038/s41467-021-24511-z>.
- [41] Y. Zeng, S. Zhang, L. Yin, Y. Dai, Electrocatalytic degradation of pesticide micropollutants in water by high energy pulse magnetron sputtered Pt/Ti anode, *Chin. Chem. Lett.* 33 (2022) 5196–5199, <https://doi.org/10.1016/j.ccllet.2022.01.031>.
- [42] X. Liu, R. Dang, W. Dong, X. Huang, J. Tang, H. Gao, G. Wang, A sandwich-like heterostructure of TiO<sub>2</sub> nanosheets with MIL-100 (Fe): a platform for efficient visible-light-driven photocatalysis, *Appl. Catal. B: Environ.* 209 (2017) 506–513, <https://doi.org/10.1016/j.apcatb.2017.02.073>.
- [43] N. Banić, B. Abramović, J. Krstić, D. Šojić, D. Lončarević, Z. Cherkezova-Zheleva, V. Guzvány, Photodegradation of thiocloprid using Fe/TiO<sub>2</sub> as a heterogeneous photo-Fenton catalyst, *Appl. Catal. B: Environ.* 107 (2011) 363–371, <https://doi.org/10.1016/j.apcatb.2011.07.037>.
- [44] K. Kosaka, H. Yamada, S. Matsui, S. Echigo, K. Shishida, Comparison among the methods for hydrogen peroxide measurements to evaluate advanced oxidation processes: application of a spectrophotometric method using copper (II) ion and 2, 9-dimethyl-1, 10-phenanthroline, *Environ. Sci. Technol.* 32 (1998) 3821–3824, <https://doi.org/10.1021/es9800784>.
- [45] L. Santos-Juanes, J.G. Sánchez, J.C. López, I. Oller, S. Malato, J.S. Pérez, Dissolved oxygen concentration: A key parameter in monitoring the photo-Fenton process, *Appl. Catal. B: Environ.* 104 (2011) 316–323, <https://doi.org/10.1016/j.apcatb.2011.03.013>.
- [46] M. Wu, S. Song, T. Wang, W. Sun, S. Xu, Y. Yang, Natural sphalerite photocatalyst for treatment of oily wastewater produced by solvent extraction from spent lithium-ion battery recycling, *Appl. Catal. B: Environ.* 313 (2022), 121460, <https://doi.org/10.1016/j.apcatb.2022.121460>.
- [47] Y. Wei, G. Lu, D. Xie, T. Sun, Y. Liu, Y. Zhang, J. An, M. Li, H. Guo, Degradation of enrofloxacin in aqueous by DBD plasma and UV: degradation performance, mechanism and toxicity assessment, *Chem. Eng. J.* 431 (2022), 133360, <https://doi.org/10.1016/j.cej.2021.133360>.
- [48] W. Xiang, M. Huang, X. Wu, F. Zhang, D. Li, T. Zhou, Amplification effects of magnetic field on hydroxylamine-promoted ZVI/H<sub>2</sub>O<sub>2</sub> near-neutral Fenton like system, *Chin. Chem. Lett.* 33 (2022) 1275–1278, <https://doi.org/10.1016/j.ccllet.2021.07.072>.
- [49] F.F. Dias, A.A. Oliveira, A.P. Arcanjo, F.C. Moura, J.G. Pacheco, Residue-based iron catalyst for the degradation of textile dye via heterogeneous photo-Fenton, *Appl. Catal. B: Environ.* 186 (2016) 136–142, <https://doi.org/10.1016/j.apcatb.2015.12.049>.
- [50] C. Du, Y. Zhang, Z. Zhang, L. Zhou, G. Yu, X. Wen, T. Chi, G. Wang, Y. Su, F. Deng, Fe-based metal organic frameworks (Fe-MOFs) for organic pollutants removal via photo-Fenton: a review, *Chem. Eng. J.* 431 (2022), 133932, <https://doi.org/10.1016/j.cej.2021.133932>.
- [51] Z. Wang, C. Lai, L. Qin, Y. Fu, J. He, D. Huang, B. Li, M. Zhang, S. Liu, L. Li, ZIF-8-modified MnFe<sub>2</sub>O<sub>4</sub> with high crystallinity and superior photo-Fenton catalytic activity by Zn-O-Fe structure for TC degradation, *Chem. Eng. J.* 392 (2020), 124851, <https://doi.org/10.1016/j.cej.2020.124851>.
- [52] Y. Ahmed, Z. Yaakob, P. Akhtar, Degradation and mineralization of methylene blue using a heterogeneous photo-Fenton catalyst under visible and solar light irradiation, *Catal. Sci. Technol.* 6 (2016) 1222–1232, <https://doi.org/10.1039/C5CY01494H>.
- [53] Q. Zhao, C.-C. Wang, P. Wang, Effective norfloxacin elimination via photo-Fenton process over the MIL-101(Fe)-NH<sub>2</sub> immobilized on α-Al<sub>2</sub>O<sub>3</sub> sheet, *Chin. Chem. Lett.* 33 (2022) 4828–4833, <https://doi.org/10.1016/j.ccllet.2022.01.033>.
- [54] Y. Huang, M. Kong, D. Westerman, E.G. Xu, S. Coffin, K.H. Cochran, Y. Liu, S. D. Richardson, D. Schlenk, D.D. Dionysiou, Effects of HCO<sub>3</sub> on degradation of toxic contaminants of emerging concern by UV/NO<sub>3</sub>, *Environ. Sci. Technol.* 52 (2018) 12697–12707, <https://doi.org/10.1021/acs.est.8b04383>.
- [55] J. Fang, Y. Fu, C. Shang, The roles of reactive species in micropollutant degradation in the UV/free chlorine system, *Environ. Sci. Technol.* 48 (2014) 1859–1868, <https://doi.org/10.1021/es4036094>.
- [56] M. Khajeh, M.M. Amin, A. Fatehizadeh, T.M. Aminabhavi, Synergetic degradation of atenolol by hydrodynamic cavitation coupled with sodium persulfate as zero-waste discharge process: effect of coexisting anions, *Chem. Eng. J.* 416 (2021), 129163, <https://doi.org/10.1016/j.cej.2021.129163>.
- [57] X. Yang, F.L. Rosario-Ortiz, Y. Lei, Y. Pan, X. Lei, P. Westerhoff, Multiple roles of dissolved organic matter in advanced oxidation processes, *Environ. Sci. Technol.* 56 (2022) 11111–11131, <https://doi.org/10.1021/acs.est.2c01017>.
- [58] E.A. Vialyk, G. McKay, F.L. Rosario-Ortiz, Computational assessment of the three-dimensional configuration of dissolved organic matter chromophores and influence on absorption spectra, *Environ. Sci. Technol.* 54 (2020) 15904–15913, <https://doi.org/10.1021/acs.est.0c05860>.
- [59] S.R. Pouran, A.A. Aziz, W.M.A.W. Daud, Review on the main advances in photo-Fenton oxidation system for recalcitrant wastewaters, *J. Ind. Eng. Chem.* 21 (2015) 53–69, <https://doi.org/10.1016/j.jiec.2014.05.005>.
- [60] H. Yu, G. Liu, L. Shen, R. Jin, J. Zhou, H. Guo, L. Wang, Facile preparation of coprecipitates between iron oxides and dissolved organic matter for efficient Fenton-like degradation of norfloxacin, *J. Hazard. Mater.* 444 (2023), 130394, <https://doi.org/10.1016/j.jhazmat.2022.130394>.
- [61] C. Zhao, L. Meng, H. Chu, J.-F. Wang, T. Wang, Y. Ma, C.-C. Wang, Ultrafast degradation of emerging organic pollutants via activation of peroxydisulfate over Fe<sub>3</sub>C/Fe@N-C<sub>x</sub>: singlet oxygen evolution and electron-transfer mechanisms, *Appl. Catal. B: Environ.* 321 (2023), 122034, <https://doi.org/10.1016/j.apcatb.2022.122034>.
- [62] A. Aleboey, M.E. Olya, H. Aleboey, Electrical energy determination for an azo dye decolorization and mineralization by UV/H<sub>2</sub>O<sub>2</sub> advanced oxidation process, *Chem. Eng. J.* 137 (2008) 518–524, <https://doi.org/10.1016/j.cej.2007.05.016>.
- [63] V. Romero, O. González, B. Bayarri, P. Marco, J. Giménez, S. Esplugas, Degradation of Metoprolol by photo-Fenton: comparison of different photoreactors performance, *Chem. Eng. J.* 283 (2016) 639–648, <https://doi.org/10.1016/j.cej.2015.07.091>.
- [64] A. De Luca, R.F. Dantas, S. Esplugas, Assessment of iron chelates efficiency for photo-Fenton at neutral pH, *Water Res.* 61 (2014) 232–242, <https://doi.org/10.1016/j.watres.2014.05.033>.
- [65] D.H. Funaí, F. Didier, J. Giménez, S. Esplugas, P. Marco, A.M. Junior, Photo-Fenton treatment of valproate under UVC, UVA and simulated solar radiation, *J. Hazard. Mater.* 323 (2017) 537–549, <https://doi.org/10.1016/j.jhazmat.2016.06.034>.
- [66] Y. Jin, L. Wang, Y. Song, J. Zhu, M. Qin, L. Wu, P. Hu, F. Li, L. Fang, C. Chen, Integrated life cycle assessment for sustainable remediation of contaminated agricultural soil in China, *Environ. Sci. Technol.* 55 (2021) 12032–12042, <https://doi.org/10.1021/acs.est.1c02535>.
- [67] H. Dong, N. Song, M. Yan, H. Wu, H. Zhang, C. Ma, Y. Wang, Fabrication of HRP/Bi<sub>2</sub>WO<sub>6</sub> photoenzyme-coupled artificial catalytic system for efficiently degrading bisphenol A, *Chin. Chem. Lett.* 32 (2021) 2047–2051, <https://doi.org/10.1016/j.ccllet.2020.11.015>.
- [68] B. Song, Y. Zhou, H.-M. Yang, J.-H. Liao, L.-M. Yang, X.-B. Yang, E. Ganz, Two-dimensional Anti-Van't Hoff/Le Bel array AlB<sub>6</sub> with high stability, unique motif, triple dirac cones, and superconductivity, *J. Am. Chem. Soc.* 141 (2019) 3630–3640, <https://doi.org/10.1021/jacs.8b13075>.
- [69] Y. Wu, X. Li, H. Zhao, F. Yao, J. Cao, Z. Chen, F. Ma, D. Wang, Q. Yang, 2D/2D FeNi-layered double hydroxide/bimetal-MOFs nanosheets for enhanced photo-Fenton degradation of antibiotics: Performance and synergetic degradation mechanism, *Chemosphere* 287 (2022), 132061, <https://doi.org/10.1016/j.chemosphere.2021.132061>.
- [70] Q. Zou, Z. Zhang, H. Li, W. Pei, M. Ding, Z. Xie, Y. Huo, H. Li, Synergistic removal of organic pollutant and metal ions in photocatalysis-membrane distillation system, *Appl. Catal. B: Environ.* 264 (2020), 118463, <https://doi.org/10.1016/j.apcatb.2019.118463>.
- [71] Q. Zhang, Z. Zhang, D. Zhao, L. Wang, H. Li, F. Zhang, Y. Huo, H. Li, Synergistic photocatalytic-photothermal contribution enhanced by recovered Ag<sup>+</sup> ions on MXene membrane for organic pollutant removal, *Appl. Catal. B: Environ.* 320 (2023), 122009, <https://doi.org/10.1016/j.apcatb.2022.122009>.
- [72] Y.-X. Li, X. Wang, C.-C. Wang, H. Fu, Y. Liu, P. Wang, C. Zhao, S-TiO<sub>2</sub>/UiO-66-NH<sub>2</sub> composite for boosted photocatalytic Cr (VI) reduction and bisphenol A degradation under LED visible light, *J. Hazard. Mater.* 399 (2020), 123085, <https://doi.org/10.1016/j.jhazmat.2020.123085>.
- [73] C. Zhao, Z. Wang, X. Li, X. Yi, H. Chu, X. Chen, C.-C. Wang, Facile fabrication of BUC-21/Bi<sub>2</sub>O<sub>3</sub>/Br<sub>10</sub> composites for enhanced photocatalytic Cr (VI) reduction

- under white light, Chem. Eng. J. 389 (2020), 123431, <https://doi.org/10.1016/j.cej.2019.123431>.
- [74] A. Wang, H. Wang, H. Deng, S. Wang, W. Shi, Z. Yi, R. Qiu, K. Yan, Controllable synthesis of mesoporous manganese oxide microsphere efficient for photo-Fenton-like removal of fluoroquinolone antibiotics, Appl. Catal. B: Environ. 248 (2019) 298–308, <https://doi.org/10.1016/j.apcatb.2019.02.034>.
- [75] R. Su, L. Huang, N. Li, L. Li, B. Jin, W. Zhou, B. Gao, Q. Yue, Q. Li, Chlorine dioxide radicals triggered by chlorite under visible-light irradiation for enhanced degradation and detoxification of norfloxacin antibiotic: radical mechanism and toxicity evaluation, Chem. Eng. J. 414 (2021), 128768, <https://doi.org/10.1016/j.cej.2021.128768>.